

AD-A071 656

ATOMIC ENERGY RESEARCH ESTABLISHMENT HARWELL (ENGLAND)

F/G 11/6

ELECTRON MICROSCOPE IMAGE CONTRAST FROM SMALL DISLOCATION LOOPS--ETC(U)

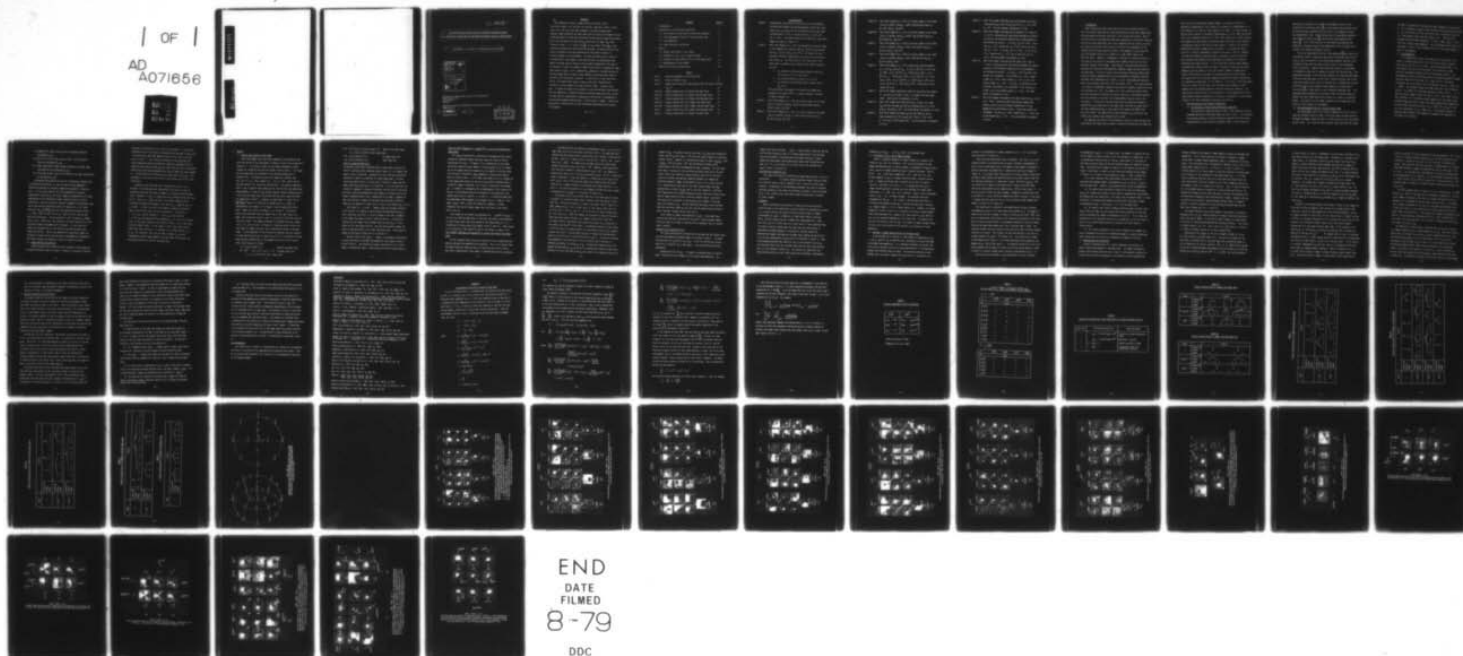
FEB 79 S M HOLMES, B L EYRE, C A ENGLISH

UNCLASSIFIED

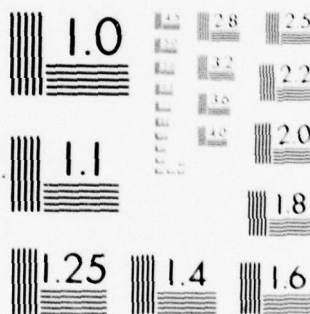
AERE-R-9307

NL

| OF |
AD
A071656



END
DATE
FILMED
8-79
DDC



MICROCOPY RESOLUTION TEST CHART
NATIONAL BUREAU OF STANDARDS-1963-A

ADA 021 656

DGC FILE COPY

6

Electron Microscope Image Contrast from Small Dislocation Loops:III. Theoretical Predictions for Non-Edge Dislocation Loops in a BCC Crystal

10

S.M./Holmes,* B.L./Eyre, C.A./English and R.C./Perrin*

Accession For	
NTIS G.M.&I	<input checked="" type="checkbox"/>
DDC TAB	<input type="checkbox"/>
Unannounced	<input type="checkbox"/>
Justific ti.	<input type="checkbox"/>
By _____	
Distribution/ _____	
Availability Codes	
Dist	Avail and/or special
A	

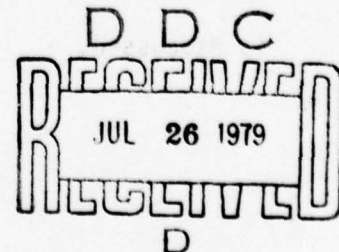
*Department of Metallurgy and Science of Materials,
Oxford University,
Parks Road,
Oxford.

Metallurgy Division and Theoretical Physics Division,
AERE Harwell.

11 Feb 1979

HL79/500 (C.16)

12 57p.



046 500

ABSTRACT

↓ The theoretical study of image contrast from small finite dislocation loops in an isotropic bcc crystal, reported in Parts I and II (Eyre et al 1977 a,b), has been extended to include non-edge loops. Computer image simulation has again been used to study the influence of loop normal, (n), Burger's vector, (b), diffraction vector, (g), and image plane normal, (z), on the distribution of black-white intensities in images from loops located in Layer 1, i.e. within $0.25 \frac{\epsilon}{g}$ of the surface, where $\frac{\epsilon}{g}$ is the extinction distance for the diffracting vector (g). As before, the choice and range of parameters have been determined by the authors interest in radiation damage in bcc molybdenum. The main conclusion from a survey of non-edge perfect loop images is that modifications are predicted to the images from edge loops on going to the non-edge configuration, but that in the majority of cases the scheme of image classification introduced for edge loops based on $|g \cdot b|$ is still appropriate. Generally, the modifications to the edge images take the form of some skewing of the black-white lobes or rotation of the black-white interface. In particular, it was found that, firstly, the images where $|g \cdot b| > 1$ always retain their characteristic interface structure between the black and white lobes. Secondly, the $g \cdot b = 0$ images from loops with b normal to z may be distorted significantly from the symmetrical "butterfly" obtained from pure edge loops and, thirdly, for some specific combinations of g, b, n and z difficulty is encountered in distinguishing between modified $g \cdot b = 0$ and $0 < |g \cdot b| < 1$ images. Lastly, the application of these results to the experimental determination of b and n is discussed.

* ϵ psilon

	<u>CONTENTS</u>	<u>Page No</u>
1.	Introduction	1
2.	Calculation of the Electron Intensities	2
2.1	The solution of the electron diffraction equations	2
2.2	The displacement field of a finite circular loop	3
2.3	Loop geometries	4
2.4	Image contrast calculations	5
3.	Results	7
3.1	General description of the images	7
3.2	Influence of $ \underline{g} \times \underline{b} $ on Image Strength	13
3.3	Problems in Image Identification for Non-edge loops	13
3.4	Determination of loop Normal	15
4.	General Discussion and Conclusions	19

	<u>TABLES</u>	
Table 1	Contrast parameters (100 kV electrons)	27
Table 2	Values of moduli of $\underline{g}, \underline{b}$	28
Table 3	Image Classification for Edge Loops within the Layer structure ($w_g \sim 0$)	29
Table 4a	Figures showing Case (I) Images from Edge loops	30
Table 4b	Figures showing Case (I) Images from Non-edge loops	30
Table 5	Figures showing Case (II) Images from Non-edge loops	31
Table 6a	Figures showing Case (III) Images from Edge loops	32
Table 6b	Figures showing Case (III) Images from Non-Edge loops	33
Table 7	Figures showing Case (IV) Images from Non-Edge loops	34
Table 8	Figures showing Case (V) Images from Edge loops	34

ILLUSTRATIONS

Figure 1 Stereographic projections illustrating the crystallographic relationships between the possible Burgers vectors (\underline{b}), loop normal (\underline{n}_1 , \underline{n}_2 and \underline{n}_3) and the diffracting vectors (\underline{g}) under consideration in a B.C.C. crystal with (a) $\underline{z} = [011]$ and (b) $\underline{z} = [001]$. The symbol Θ specifies dislocation loops whose images are shown in figures 2-7.

Figure 2 Dark field images at $\underline{z} = [011]$ corresponding to various stages in the formation of a perfect loop $\underline{b}_2 = \frac{a}{2} [\bar{1}1\bar{1}]$ from faulted loops $\underline{b}_1 = \frac{a}{2} [01\bar{1}]$ and $\underline{b}_1 = \frac{a}{2} [\bar{1}10]$. The images (i)-(vii) represent different combinations of \underline{b} and \underline{n} for each diffraction vector, \underline{g} . The loop normal or its projection in the image plane is marked on each image and the three directions of \underline{n} are:

1. \underline{n}_1 , parallel to the nucleation Burgers vector \underline{b}_1 , ((i) and (iii) or (ii) and (iv)).
2. \underline{n}_2 , mid-way between \underline{n}_1 and \underline{n}_3 ((v) or (vi))
3. \underline{n}_3 , parallel to the perfect loop Burgers vector \underline{b}_2 , (vii).

The scale marker corresponds to 10 nm and the computation parameters are given in §2.4. A similar system of notation is used in Figures 3-7.

Figure 3 Dark field images at $\underline{z} = [011]$ of various stages in the formation of a perfect loop $\underline{b}_2 = \frac{a}{2} [\bar{1}1\bar{1}]$ from faulted loops $\underline{b}_1 = \frac{a}{2} [011]$ and $\underline{b}_1 = \frac{a}{2} [\bar{1}10]$.

Figure 4 Dark field images at $\underline{z} = [011]$ of various stages in the formation of a perfect loop $\underline{b}_2 = a[100]$ from faulted loops $\underline{b}_1 = \frac{a}{2} [101]$ and $\underline{b}_1 = \frac{a}{2} [110]$.

- Figure 5A Dark field images at $\underline{z} = [011]$ of various stages in the formation of a perfect loop $\underline{b}_2 = a[010]$ from faulted loops $\underline{b}_1 = \frac{a}{2} [01\bar{1}]$ and $\underline{b}_1 = \frac{a}{2} [011]$.
- Figure 5B Dark field images at $\underline{z} = [011]$ of various stages in the formation of a perfect loop $\underline{b}_2 = a[010]$ from faulted loops $\underline{b}_1 = \frac{a}{2} [\bar{1}10]$ and $\underline{b}_1 = \frac{a}{2} [110]$.
- Figure 6 Dark field images at $\underline{z} = [001]$ of various stages in the formation of a perfect loop $\underline{b}_2 = [010]$ from faulted loops $\underline{b}_1 = \frac{a}{2} [011]$ and $\underline{b}_1 = \frac{a}{2} [110]$.
- Figure 7 Dark field images at $\underline{z} = [001]$ of various stages in the formation of a perfect loop $\underline{b}_2 = [001]$ from faulted loops $\underline{b}_1 = \frac{a}{2} [011]$ and $\underline{b}_1 [101]$.
- Figure 8 Dark field images at $\underline{z} = [011]$ showing the relation between \underline{g} , \underline{b} , \underline{b}_p , and \underline{n} or \underline{n}_p . In (a) $\underline{b} = \frac{a}{2} [\bar{1}11]$, $\underline{n} = [\bar{1}11]$ and $\underline{g} = 200$; (b) $\underline{b} = \frac{a}{2} [\bar{1}11]$, $\underline{n} = [\bar{1}10]$ and $\underline{g} = 200$; (c) $\underline{b} = \frac{a}{2} [\bar{1}11]$, $\underline{n} = [\bar{1}10]$ and $\underline{g} = 21\bar{1}$; (d) $\underline{b} = \frac{a}{2} [\bar{1}11]$, $\underline{n} = [\bar{1}10]$ and $\underline{g} = 211$; (e) $\underline{b} = \frac{a}{2} [\bar{1}1\bar{1}]$, $\underline{n} = [01\bar{1}]$ and $\underline{g} = 01\bar{1}$, and in (f) $\underline{b} = \frac{a}{2} [\bar{1}1\bar{1}]$, $\underline{n} = [01\bar{1}]$ and $\underline{g} = 21\bar{1}$. Scale marker corresponds to 10 nm.
- Figure 9 Dark field images showing the effect of increasing the product of $|\underline{g}|$ and $|\underline{b}|$ on type 2 ($|\underline{g} \cdot \underline{b}| = 0$) images from pure edge loops. Scale marker corresponds to 10 nm.
- Figure 10 Dark field images from loops having $\underline{b}_2 = a[010]$ in an edge (\underline{n}_3) and two non-edge (\underline{n}_2 and \underline{n}_1) configurations at $\underline{z} = [011]$ with $\underline{g} = 200$ and $\underline{g} = 211$. The scale marker corresponds to 10 nm.
- Figure 11 Dark field images from edge (\underline{n}_3) and non edge (\underline{n}_2 and \underline{n}_1) loops having $\underline{b}_2 = \frac{a}{2} [\bar{1}1\bar{1}]$ and $\underline{b}_2 = \frac{a}{2} [11\bar{1}]$ at $\underline{z} = [011]$ with $\underline{g} = 21\bar{1}$ and $\underline{g} = 200$ respectively. The scale marker corresponds to 10 nm.

- Figure 12 Dark field images from edge (\underline{n}_3) and non-edge (\underline{n}_1 and \underline{n}_2) loops having $\underline{b}_2 = a[010]$ and $\underline{b}_2 = \frac{a}{2} [1\bar{1}1]$ at $z = [011]$ with $g = 21\bar{1}$. The scale marker corresponds to 10 nm.
- Figure 13 Dark field images from edge and non edge $\frac{a}{2} \langle 111 \rangle$ loops at $z = [011]$ illustrating the relationship between the vectors \underline{n} and \underline{m} for the different combinations of loop geometries and diffraction vectors. In (a) $\underline{b}_2 = \frac{a}{2} [11\bar{1}]$ with: first row, $\underline{n}_3 = [11\bar{1}]$, second row, $\underline{n}_1 = [01\bar{1}]$, and in the third row, $\underline{n}_1 = [110]$. In (b) $\underline{b}_2 = \frac{a}{2} [111]$ with: first row $\underline{n}_3 = [111]$, second row, $\underline{n}_1 = [011]$ and in the third row, $\underline{n}_1 = [110]$. The scale marker corresponds to 10 nm.
- Figure 14 Dark field images from edge and non edge $a\langle 100 \rangle$ loops at $z = [011]$ illustrating the relationships between the vectors \underline{n} and \underline{m} for the different combinations of loop geometries and diffraction vectors. In (a) $\underline{b}_2 = a[010]$ and four loop normals are considered: first column, $\underline{n}_3 = [010]$, second column, $\underline{n}_1 = [01\bar{1}]$, third column, $\underline{n}_1 = [011]$, and in the fourth column, $\underline{n}_1 = [110]$. In (b) $\underline{b}_2 = a[100]$ loop and two different loop normals are considered: first column, $\underline{n}_3 = a[100]$, and in the second column, $\underline{n}_1 = [110]$. The scale marker corresponds to 10 nm.
- Figure 15 Dark field images from edge and non edge loops with $\underline{b}_2 = a[100]$ at $z = [001]$ illustrating the relationships between the vectors \underline{n} and \underline{m} for the different combinations of loop geometries and diffraction vectors. Three loop normals are considered: top row, $\underline{n}_3 = [100]$, middle row, $\underline{n}_1 = [100]$, and in the bottom row $\underline{n}_1 = [101]$. The scale marker corresponds to 10 nm.

1. Introduction

Small dislocation loops lying close to the top or bottom surface of a thin foil exhibit characteristic black-white (B-W) contrast when imaged under strong two-beam diffraction conditions in the electron microscope. Much of the early work on B-W images was based upon theoretically calculated intensity profiles for pure edge loops, and it was suggested that the vector $\underline{\ell}$ joining the centre of the black lobe to that of the white was independent of the imaging reflection \underline{g} and parallel (within a few degrees) to the projection \underline{b}_p of the Burgers vector \underline{b} (e.g. Rühle et al 1965, Rühle 1967a,b and McIntyre, 1967). However, a fundamental limitation of intensity profiles is that they do not expose the two-dimensional symmetry which can be such an important feature of B-W images. More recently, two approaches have been developed for displaying two-dimensional computed images from both edge and non-edge loops. The first involves calculating equi-intensity contour maps which may then be compared directly with experimental micrographs (Wilkins and Rühle 1972, Häussermann et al 1972), or with a two-dimensional densitometer trace obtained from these (Föll and Wilkins, 1977). The second approach is to obtain a photographic negative from a grid of computed intensities which are displayed on a C.R.T. unit (Maher et al 1971, Saldin and Whelan 1975). Care must be taken to calibrate the optical density on the computed negative with the response to electrons of the photographic emulsion used in the microscope. In this way it has been shown that the $\underline{\ell}$ -analysis method of determining \underline{b} can break down for non-edge loops, and even for edge loops if the angle between \underline{g} and \underline{b}_p is large (Eyre 1972, Wilkins and Rühle 1972, Eyre et al 1974). The quantitative relation between $\underline{\ell}$, \underline{g} , \underline{b} and the loop normal \underline{n} has recently been examined by Ohr (1976).

An important conclusion of the theoretical studies is that by observing experimental B-W images using a number of operating reflections and comparing

these with the corresponding computed images, it should be possible to determine \underline{b} unambiguously, and to obtain an estimate of \underline{n} (Häussermann et al 1972, Holmes et al 1976, Ohr 1976, English et al 1978). In recent studies by Wilkens and co-workers at Stuttgart (Häussermann et al 1972, Jäger and Wilkens 1975), and at Harwell (English et al 1977, 1978, Jenkins et al 1978) considerable emphasis has been placed on analysing small dislocation loops formed in irradiated bcc metals since they are more complex in terms of the possible combinations of \underline{b} and \underline{n} compared with fcc metals. In two previous papers (Eyre et al 1977a,b, subsequently referred to as Parts I and II), computer simulated B-W images of pure edge loops in isotropic bcc and fcc materials were presented and compared with experimental micrographs of irradiated molybdenum and copper crystals. It was shown that relating image symmetry from edge loops located within the layer structure to $|\underline{g} \cdot \underline{b}|$ and the angle between \underline{b} (\underline{n}) and \underline{z} where \underline{z} is the foil normal, enables a comparatively simple classification to be made of the many different possible images. In this paper (Part III) we present computer simulated B-W images representing all expected non-edge loops in a bcc material. As in Part I, the displacement field of a finite circular loop in an isotropic elastic medium is used, together with the two-beam dynamical electron diffraction equations. The application of these results to the analysis of a mixed population of small loops having different combinations of \underline{b} and \underline{n} is presented in a fourth paper (English et al 1979) subsequently referred to as Part IV.

2. The Calculation of the Electron Intensities

2.1 The Solution of the Electron Diffraction Equations

The theoretical images presented in Part I were computed using the programme described by Bullough, Maher and Perrin (1971). This employed the two-beam dynamical electron diffraction equations with the column approximation as given by Howie and Whelan (1961), in the form which

requires the derivative of the defect displacement field \underline{R} in the direction of the electron beam $-\frac{dR}{dz}$. In the present work two other forms of the diffraction equations were also tried in an attempt to reduce the computational time: the alternative set of Howie-Whelan equations which require \underline{R} rather than $\frac{dR}{dz}$, and the Bloch wave equations which employ $\frac{dR}{dz}$. In all three versions of the program the equations were numerically integrated down the two-dimensional grid of columns with a variable step-length Kutta-Merson routine.

Of the two Howie-Whelan versions, that employing $\frac{dR}{dz}$ was found to be considerably faster in operation, mainly due to the time taken calculating sin and cos functions in the diffraction equations section of the \underline{R} formalism (there was also some saving of time in the displacement field calculation). However, both these forms require a large number of integration steps even in regions of crystal far from the loop. This problem was overcome in the Bloch-wave program since the wave amplitudes, unlike the beam amplitudes, do not vary in perfect crystal, and so very large step lengths can be used far from the loop. Although the electron diffraction part of the program is more complex, the time saved in calculating $\frac{dR}{dz}$ at fewer points in the integration outweighs this. This advantage would presumably be even greater when calculating images of defects with more complicated strain fields (e.g. loops in anisotropic media). The majority of the images presented in this paper were computed with this version of the program.

2.2 The Displacement Field of a Finite Circular Loop

The displacement field in an isotropic medium of a finite circular edge loop (Burgers vector \underline{b} normal to the loop plane) has been given by Bullough and Newman (1960) and that of a shear loop (\underline{b} in the loop plane) by Ohr (1972). For a loop of mixed character these solutions may simply

be added in proportion to the edge and shear components of the desired \underline{b} . It is important to adopt a sign convention for \underline{b} and the loop normal \underline{n} . The line direction of the dislocation loop is defined as positive in a right-handed screw sense with respect to \underline{n} . Then \underline{b} can be assigned using the FS/RH convention. If this is done, $|\underline{b} \cdot \underline{n}| > 0$ for a loop with a vacancy edge component. The displacement field itself, and the manner in which it was formulated for use in the image program is given in the Appendix.

2.3 Loop Geometries

It is expected that loops in bcc metals will nucleate on $\{110\}$ planes as faulted loops with $\underline{b} = \frac{a}{2} \langle 110 \rangle$ and then shear to perfect loops with $\underline{b} = \frac{a}{2} \langle 111 \rangle$ or $\underline{b} = a \langle 100 \rangle$ (Eyre and Bullough 1965); the loop normals are either in the original $\langle 110 \rangle$ direction or some direction intermediate between this and the Burgers vector \underline{b} . The experimentally useful diffracting vectors for obtaining dynamical images from such loops are of the type $\langle 110 \rangle$, $\langle 200 \rangle$ and $\langle 211 \rangle$ and these reflections can be obtained at foil orientations close to $\underline{z} = [011]$ and $\underline{z} = [001]$. The simulated images from edge loops with such diffracting vectors in an $[011]$ foil have been reported in Parts I and II. In this paper we present images for $\frac{a}{2} \langle 110 \rangle$, $\frac{a}{2} \langle 111 \rangle$ and $a \langle 100 \rangle$ loops lying on their possible $\{110\}$ nucleation planes together with the perfect loops rotated halfway and fully to their pure edge configurations imaged with the same three diffracting vectors in a $\underline{z} = [011]$ foil and with $\langle 110 \rangle$ and $\langle 200 \rangle$ reflections in a $\underline{z} = [001]$ foil. The procedure adopted to identify these different loop geometries throughout the remainder of this paper is as follows:-

- (i) Edge $\frac{a}{2} \langle 110 \rangle$ loops lying on their nucleation plane are designated $\underline{n}_1, \underline{b}_1$.
- (ii) $\frac{a}{2} \langle 111 \rangle$ or $a \langle 100 \rangle$ loops lying on their $\{110\}$ nucleation plane are designated $\underline{n}_1, \underline{b}_2$.
- (iii) These same perfect loops rotated halfway to a perfect edge configuration are designated $\underline{n}_2, \underline{b}_2$.
- (iv) These same perfect loops fully rotated to an edge configuration are designated $\underline{n}_3, \underline{b}_2$.

Stereograms representing the two foil orientations together with the operating reflections, \underline{g} , and the possible loop geometries identified according to the above scheme are presented in figures 1a and b. In the survey figures (2-7) only geometrically distinct combinations of $\underline{b}, \underline{n}$ and \underline{g} are given; images corresponding to all other combinations can be obtained by simple rotations and/or by mirror reflections. With one exception, because of geometric equivalence, only two of the possible nucleation planes are required, e.g. for loops shearing to $\underline{b}_2 = \frac{a}{2} [\bar{1}1\bar{1}]$ there are three possible nucleation planes, $\underline{n}_1 = (\bar{1}10), (\bar{1}0\bar{1})$ or $(01\bar{1})$, but at $\underline{z} = [011]$ the first two are geometrically equivalent. The one exception is the inclined $\underline{b}_2 = a[010]$ loop in the $\underline{z} = [011]$ foil (see figure 1a) for which three of the $\{110\}$ nucleation planes are geometrically different. In this case only, images are presented for all four possible nucleation planes (see figures 5A and 5B). Some of the geometrically equivalent images are included in figures (8-15) and the actual loop geometries presented in the survey figures are denoted by circles in figures 1a and 1b.

2.4 Image Contrast Calculations

Bright and dark field intensities were obtained for both edge and non-edge dislocation loops of radius r located at a distance d from the

electron exit surface of a bcc crystal of thickness t . The contrast parameters used in the present calculations are the same as those used in previous work (Bullough, Maher and Perrin 1971, Part I) and are given in Table 1. The extinction distances are the two-beam, 0°K values reported by Howie and Basinski (1968) for molybdenum and the anomalous absorption distances ξ_g^* were taken from the curve of two-beam, 300°K values published by Humphreys and Hirsch (1968) for atomic number 41. The mean absorption distance ξ_0^* was taken equal to $\frac{2}{3} \xi_{110}^*$; this assignment is not too critical since it only affects the scale of the intensities.

Compared to the pure edge loops considered in Part I, it is necessary to include many more combinations of \underline{b} and \underline{n} in order to adequately represent the range of images to be expected from non-edge loops. Moreover, in Part I, images were only presented for $\frac{a}{2} \langle 110 \rangle$ and $\frac{a}{2} \langle 111 \rangle$ loops at $\underline{z} = [011]$, whereas in this paper images are also presented for edge and non-edge $a \langle 100 \rangle$ loops at $\underline{z} = [001]$ as well as $\underline{z} = [011]$. In order to restrict the number of images calculations were carried out for only one set of parameters:- loop radius $r = 0.1 \xi_{110}$, crystal thickness $t = 5.25 \xi_{110}$, loop position $d = 0.15 \xi_{110}$ and Bragg deviation parameter $\omega_g = 0$. Thus, all calculations are for loops located at the centre of layer 1 (L_1) in the layer structure (Ruhle 1967a). It was shown in Part I that loop location within the layer structure, i.e. whether it is located within L_1 , L_2 or L_3 , foil thickness, loop size and small changes in ω_g do not fundamentally affect image symmetry for edge loops and we expect the same generalisation to hold for non-edge loops.

3. Results

3.1 General description of the images

Dark field images from loops whose geometries are defined by the encircled points on the stereograms in figures 1a and 1b are presented in figures 2-7. The values of $|\underline{g} \cdot \underline{b}|$ for the loops considered in these figures are listed for the two foil normals used in Table 2. The images for pure edge loops are presented in the top and bottom rows of Figures (2-7); the bottom row gives the images of a perfect loop ($\underline{b}_2 = \frac{a}{2} \langle 111 \rangle$ or a $\langle 100 \rangle$) imaged at $\underline{z} = \langle 011 \rangle$ or $\langle 001 \rangle$, while the top row shows the $\frac{a}{2} \langle 110 \rangle$ from which they may form. The approach adopted in Parts I and II towards these images was to classify their two dimensional image symmetry in terms of $|\underline{g} \cdot \underline{b}|$ and the angular relation between \underline{b} and \underline{z} ; in this way the images were classified into four basic types and these are summarized in Table 3. Examples of image types 2, 3 and 4 for an $\frac{a}{2} [\bar{1}1\bar{1}]$ edge loop at $\underline{z} = [011]$ and an $a [010]$ loop at $\underline{z} = [001]$ are represented by the images vii in figures 2 and 6 respectively, while type 1 images are seen in the images (i) in figure 3. The present results have confirmed that the images from a $\langle 100 \rangle$ edge loops at $\underline{z} = [001]$, not considered in Parts I and II, can also be classified into the four basic types. The images presented in the middle two rows (images (iii), (v), (iv) and (vi)) in figures 2-7 show the extent to which the four types of images from edge loop are modified on going to non-edge loops. In the remainder of this section we highlight the main features of these modifications and in order to do this it is convenient to break down the many combinations of loop geometries and foil plane normals into 5 basic groups as follows:-

- (I) \underline{b} and \underline{n} normal to \underline{z} edge and non-edge loops
(II) $90^\circ > \angle(\underline{b}, \underline{z})$ or $\angle(\underline{n}, \underline{z}) > 0^\circ$ non-edge loops only
i.e. \underline{b} or \underline{n} inclined to the image plane.

(III) $90^\circ > [\angle (b, z) \text{ and } \angle (n, z)] > 0^\circ$ edge and non-edge loops.
i.e. b and n inclined to the image plane.

(IV) b or n parallel to z non-edge loops only

(V) b and n parallel to z edge loops only

Case (I) b and n normal to z

The present results have confirmed that all edge loops (perfect and faulted) satisfying this condition exhibit types 2, 3 or 4 images (see images listed in Table 4a). Rotation of n out of the b-z plane while retaining n normal to z modifies all three image types. The most significant modification is to the type 2 'butterfly' image (see the images identified under $g.b = 0$ in Table 4b). It can be seen that the 'butterfly' symmetry is severely distorted, with one pair of the white and black lobes being enhanced at the expense of the other giving the image an appearance more like a skewed type 3 B-W image. Examples of edge loop 'butterfly' images and non-edge loop distorted 'butterfly' images can be compared in figure 2(a) vii and iii and figure 6(a) vii & iv.

With regard to $0 < |g.b| \leq 1$ images, going to non-edge configurations results in a skewing of the B-W lobes and some modification in their interface, but there is no basic change in the type 3 symmetry of the image (see images listed in Tables 4a and b). Of particular interest are the images from non-edge loops for which $g.n = 0$ (see figure 2(c)iii and figure 6(b)iv); they are both severely skewed and there is some distortion of the black and white lobes. These types of images are discussed in more detail in section 3.3.

The basic form of the $|g.b| > 1$ image is not changed significantly on going from edge to non-edge loop geometries (see images listed in Tables 4a and b). The interface structure characteristic of a type 4 image is retained but there is some skewing of the B-W lobes towards n.

Case (II) $90^\circ > [\angle(b,z) \text{ or } \angle(n,z)] > 0^\circ$ i.e. \underline{b} or \underline{n} inclined to the image plane

All loops satisfying this condition are non-edge and the figures showing the simulated images from such loops are listed in Table 5. Considering first $\underline{g} \cdot \underline{b} = 0$ images, if \underline{n} is rotated out of the image plane with respect to \underline{b} but remains in the \underline{b} - \underline{z} plane, or \underline{b} is rotated out of the image plane with respect to \underline{n} but remains in the \underline{n} - \underline{z} plane, then the type 2 'butterfly' image symmetry is retained (see figures 5A(c)iii, 6(a)iii and v. In all other cases where \underline{n} or \underline{b} is rotated out of the image plane and out of the \underline{b} - \underline{z} or \underline{n} - \underline{z} plane a distorted type 2 'butterfly' image is obtained. As in case (I) distortion of non-edge $\underline{g} \cdot \underline{b} = 0$ images is a consequence of an enhancement of the intensity of one pair of black-white lobes at the expense of the second pair (see figures 2(a)iv and vi, 4(b)iii, v, iv and vi). It should be noted that the enhancement effect appears to be greater for $\underline{b} = a \langle 100 \rangle$ $\underline{n} = \langle 110 \rangle$, where $\angle(\underline{n}, \underline{b}) = 45^\circ$, so that the 'butterfly' symmetry is almost completely lost and the images appear more like type 3 (see figures 4(b)iii and iv).

With regard to the images corresponding to $0 < |\underline{g} \cdot \underline{b}| < 1$ and $|\underline{g} \cdot \underline{b}| > 1$ the contrast from non-edge loops is basically the same as that predicted for edge loops, apart from some skewing of the image along \underline{n} if it is rotated out of the \underline{b} - \underline{z} plane (see images listed in Table 5). There should be no difficulty in the identification of such images as types 3 or 4.

Case (III) $90^\circ > [\angle(b,z) \text{ and } \angle(n,z)] > 0^\circ$ i.e. \underline{b} and \underline{n} inclined to the image plane

In this category both \underline{b} and \underline{n} are rotated out of the image plane and edge and non-edge loop geometries are possible. The list of figures showing images from such loops are given in Tables 6a and b and it can be seen that a comparatively large number of combinations must be considered.

Considering first the contrast corresponding to $\underline{g} \cdot \underline{b} = 0$, all of the edge loops satisfy the conditions specified in Part I for obtaining type 1 contrast and the present results confirm that this contrast is obtained for $\frac{a}{2} \langle 110 \rangle$ loops at $\underline{z} = [\bar{0}01]$ as well as for $\frac{a}{2} \langle 110 \rangle$, $\frac{a}{2} \langle 111 \rangle$ and $a \langle 100 \rangle$ loops at $\underline{z} = [01\bar{1}]$. The images from non-edge loops also exhibit type 1 contrast provided $\angle(\underline{b}, \underline{z})$ and $\angle(\underline{n}, \underline{z}) < 45^\circ$. However, significant deviation from this contrast is observed when $\angle(\underline{n}, \underline{z}) > 45^\circ$. For example in figure 5A(c)v when \underline{n} lies in the \underline{b} - \underline{z} plane and $\angle(\underline{n}, \underline{z}) = 67.5^\circ$, a 'butterfly' image is obtained. In the case where \underline{n} is rotated out of the $(\underline{b}$ - $\underline{z})$ plane and $\angle(\underline{n}, \underline{z}) = 60^\circ$ or 52° distorted images with enhanced black and white lobes and an L shaped interface are obtained (see figures 5B(c)iii, iv, v and vi). The possible confusion of such images with modified type 3 images corresponding to $0 < |\underline{g} \cdot \underline{b}| < 1$ is discussed in section 3.3.

The present results also confirm that all of the edge loops for which $0 < |\underline{g} \cdot \underline{b}| < 1$ is satisfied exhibit type 3 contrast (see the figures listed in Table 6a). Particular attention is drawn to the edge $\frac{a}{2} \langle 110 \rangle$ loops at $\underline{z} = [\bar{0}01]$ imaged with $\underline{g} = \langle 110 \rangle$ so that $|\underline{g} \cdot \underline{b}| = \frac{1}{2}$ (see figures 6(b)i and (c)i and 7(b)i and ii and (c)i and ii). As in the case of similar images from $\frac{a}{2} \langle 110 \rangle$ loops at $\underline{z} = [01\bar{1}]$ the images are truncated and the B-W interface shows even more severe cusping, e.g. compare figures 2(b)ii and 7(b)i. This again reflects the angle \underline{n} and \underline{b} make with respect to \underline{z} , being 60° in the former case and 45° in the latter. An important feature of such images is that the sense of cusping reverses on reversing the sign of $\underline{g} \cdot \underline{b}$ (compare figures 7(b)i and ii) and provided $\pm \underline{g}$ pairs of images are obtained there should be no difficulty in identifying them as type 3. On going to non-edge loop geometries (see Table 6b for list of figures) type 3 contrast is obtained provided \underline{g} lies along \underline{n}_p or \underline{b}_p . Of particular importance are the images obtained when \underline{b}_p , \underline{n}_p and \underline{g} are all rotated with respect to each other. Consider first the case when \underline{g} and \underline{n}_p are rotated in the opposite sense with

respect to \underline{b}_p . The present results show that if \underline{n}_p and \underline{g} are rotated 35° either side of \underline{b}_p and $\angle(\underline{n}, \underline{b}) = 35^\circ$ basically type 3 contrast is obtained (figure 3(d)iv). However, on increasing the angle so that $\angle(\underline{n}_p, \underline{b}_p) = 55^\circ$, $\angle(\underline{g}, \underline{b}_p) = 55^\circ$ and $\angle(\underline{n}, \underline{b}) = 45^\circ$, the B-W contrast deviates quite significantly from that corresponding to type 3 contrast. The B-W interface takes a zig-zag form and the black and white lobes split into two either side of the interface (figures 5B(a)iii and (d) iv). We shall return to consider the possible confusion between such images and distorted butterfly images corresponding to $\underline{g} \cdot \underline{b} = 0$ in a later section. It is interesting to note that as the loops rotate towards the edge configuration so that $\angle(\underline{n}_p, \underline{b}_p)$ and $\angle(\underline{n}, \underline{b})$ are reduced to $\sim 27\frac{1}{2}^\circ$ and $22\frac{1}{2}^\circ$ respectively the zig-zag interface and split lobe are virtually lost and the image reverts to type 3 contrast (figures 5B(a)v and (d)vi). The second case to consider is when \underline{g} and \underline{n}_p are rotated in the same sense with respect to \underline{b}_p . The B-W interface then takes a wavy form but the black and white lobes are not split and the image retains basically type 3 contrast (figures 5B(a)iv and (d)iii).

With regard to images corresponding to $|\underline{g} \cdot \underline{b}| > 1$ only edge loops satisfy the conditions specified for case (III). Figures showing images from such loops are listed in Table 6a and as expected, they all exhibit type 4 contrast.

Case (IV): \underline{b} or \underline{n} parallel to \underline{z} :

All loops satisfying this condition are non-edge and the figures showing the corresponding simulated images are listed in Table 7. It should be noted that for \underline{b} parallel to \underline{z} , $\underline{g} \cdot \underline{b} = 0$ for all diffracting vectors, while if \underline{n} is parallel to \underline{z} , then $|\underline{g} \cdot \underline{b}| = 1$ for the diffraction vectors considered.

Considering first the $\underline{g} \cdot \underline{b} = 0$ images, as expected they all exhibit type 1 contrast and will probably not be visible experimentally. The

images from loops satisfying $|\underline{g} \cdot \underline{b}| = 1$ exhibit type 3 contrast, but the B-W interface rotates so that it is always perpendicular to \underline{g} and some care may be needed in distinguishing such images from $\underline{g} \cdot \underline{b} = 0$ type 1 images discussed above, particularly when higher order reflections are used, e.g. $\langle 211 \rangle$ (see figures 3(c)iii and (d)iii). We consider this aspect further in section 3.2.

Case(V): \underline{b} and \underline{n} parallel to \underline{z}

All loops satisfying this condition are edge-loops and $\underline{g} \cdot \underline{b} = 0$ for all reflections. The figures showing simulated images from such loops are listed in Table 8, and as reported in Part I they all exhibit type 1 contrast. As mentioned in the preceding paragraph, the level of contrast obtained increases as the order of reflection increases so that the images for $\underline{g} = \langle 211 \rangle$ exhibit clear black-white lobes and they may be mistaken for type 3 images.

2 Analysis

Before concluding the discussion of image classification mention should be made of the traditional \underline{l} analysis method for determining \underline{b} , where \underline{l} is a vector joining the centres of black and white lobes of images corresponding to $|\underline{g} \cdot \underline{b}| > 0$ (Rühle et al 1965, Rühle 1967a,b, McIntyre 1967). Earlier studies (Wilkins & Rühle 1972, Häussermann et al 1972, Eyre 1972, Eyre et al 1974, Eyre et al 1977a (part I)) have predicted that the simple \underline{l} analysis breaks down for edge loops and loops having an appreciable non-edge component in elastically isotropic materials. Simulated B-W images from edge and non-edge loops showing the position of \underline{l} for various combinations of \underline{g} , \underline{b} and \underline{n} are presented in figure 8. These results demonstrate that the conditions for \underline{l} to be parallel to \underline{b} or \underline{b}_p are even more restrictive for non-edge loops than for edge loops and also that \underline{l} is not uniquely related to \underline{n} . The results also agree with the more detailed analysis by Ohr (1976) predicting the angular relationships

between \underline{g} , \underline{b} (or \underline{b}_p), \underline{n} (or \underline{n}_p) and \underline{z} for non-edge loops.

3.2 Influence of $|\underline{g}| \times |\underline{b}|$ on Image Strength

There is a general tendency for image strength to increase as the product of $|\underline{g}|$ and $|\underline{b}|$ increases. This is most noticeable for the images obtained when $\underline{g} \cdot \underline{b} = 0$ and an example is presented in figure 9 which shows a series of images exhibiting type 2 contrast from edge $\frac{a}{2}\langle 110 \rangle$, $\frac{a}{2}\langle 111 \rangle$ and $a\langle 100 \rangle$ loops imaged with $\langle 110 \rangle$, $\langle 200 \rangle$ and $\langle 211 \rangle$ \underline{g} 's. Further examples for $\underline{g} \cdot \underline{b} = 0$ images exhibiting type 1 contrast and for $|\underline{g} \cdot \underline{b}| = 1$ images exhibiting type 3 contrast can be seen in figures 3(a)-(d) i and 5A(a)-(d) ii and iv. It is emphasised that $|\underline{g} \cdot \underline{b}| > 1$ images exhibiting type 4 contrast are only obtained for higher order reflections, i.e. $\langle 200 \rangle$ and $\langle 211 \rangle$ and thus, there is not a noticeable effect of $|\underline{g}| \times |\underline{b}|$ on image strength. The important practical consequence of the $|\underline{g}| \times |\underline{b}|$ effect is the possible difficulty in distinguishing between strong type 1 contrast and weak type 3 contrast e.g. compare images ii & iv in figures 5A(a) & (c). However, as already emphasised in Parts I and II it is essential to achieve a match between theory and experiment for a number of \underline{g} 's and values of $|\underline{g} \cdot \underline{b}|$ before \underline{b} and \underline{n} can be assigned unambiguously to a given loop. The general conclusion to be drawn is that the $|\underline{g}| \times |\underline{b}|$ effect on image strength should not give rise to any practical difficulties in the analysis of loop geometries.

3.3 Problems in Image Identification for Non-Edge Loops

It was pointed out in Section 3.1 that images corresponding to $\underline{g} \cdot \underline{b} = 0$ and $0 < |\underline{g} \cdot \underline{b}| \leq 1$ can be modified very considerably on going from edge to non-edge loop geometries. It is important therefore to consider the difficulties that may arise due to these modifications in distinguishing between the different types of image. The possible confusion arising between type 1 and type 3 images from loops with \underline{b} or \underline{n} parallel to \underline{z}

because of the dependence of image strength on $|g| \times |b|$ has already been discussed in section 3.2.

There are three additional cases to consider. The first is a further example related to the modification of type 1 contrast corresponding to $\underline{g} \cdot \underline{b} = 0$ for inclined edge loops. An example of the change in contrast on going to non-edge loop geometries is shown by the top row of images in figure 10. As \underline{n} rotates away from \underline{b} and out of the \underline{b} - \underline{z} plane strong black and white lobes develop with some splitting of the white lobe so that the B-W interface develops an L shape when $\angle(\underline{n}, \underline{b}) = 45^\circ$ and $\angle(\underline{n}_p, \underline{b}_p) = 55^\circ$. The second set of images in the bottom row of figure 10 are for loops having the same geometries but imaged with $\underline{g} = [2\bar{1}1]$ so that $|\underline{g} \cdot \underline{b}| = 1$. In this case the B-W interface again becomes L shaped as \underline{n} rotates away from \underline{b} and there is a close similarity between the form of the $\underline{g} \cdot \underline{b} = 0$ and $|\underline{g} \cdot \underline{b}| = 1$ images when the loop lies on its $\{110\}$ nucleation plane (compare the images in column (c) of figure 10).

The second case to consider is the modification in type 2 contrast corresponding to $\underline{g} \cdot \underline{b} = 0$ for edge loops with \underline{b} normal to \underline{z} . An example is shown by the top row of images in figure 11 which are for an $\frac{a}{2} [\bar{1}1\bar{1}]$ loop. As \underline{n} is rotated away from \underline{b} about \underline{z} the intensity distribution in the three pairs of black and white lobes is considerably modified so that the images from the non-edge loops appear more like a distorted type 3 image. The interface between the most prominent black and white lobes initially becomes straight for $\angle(\underline{n}, \underline{b}) = 17\frac{1}{2}^\circ$ (figure 11b) and then develops a zig-zag as \underline{n} rotates further to $\angle(\underline{n}, \underline{b}) = 35^\circ$ (figure 11c). The second set of images in the bottom row of figure 11 is for three equivalent loop geometries but imaged with $\underline{g} = 200$ so that $|\underline{g} \cdot \underline{b}| = 1$. The greatest similarity in this case exists between the top image in column (b) with the bottom image in column (c) which is a heavily skewed type 3 contrast corresponding to $\underline{g} \cdot \underline{n} = 0$.

The third case to consider is the modification in type 3 contrast

corresponding to $|\underline{g} \cdot \underline{b}| = 1$ for edge loops. An example is shown by the top row of images in figure 12 which is for an inclined $\underline{b} = a [010]$ loop. As \underline{n} is rotated away from \underline{b} and out of the \underline{b} - \underline{z} plane there is a splitting of the black and white lobes and the B-W interface takes on a markedly zig-zag form. The bottom row of images in figure 12 is the same as the top row of figure 11 and there is clearly a close similarity between the two images in column (c) in figure 12 corresponding to $|\underline{g} \cdot \underline{b}| = 1$ and 0 respectively

It is clear therefore that considerable care must be exercised in distinguishing between images corresponding to $\underline{g} \cdot \underline{b} = 0$ and to $0 < |\underline{g} \cdot \underline{b}| < 1$ from non-edge loops. However, three general points should be emphasised.

(a) The above three cases where confusion can arise are when \underline{g} , \underline{b} , and \underline{n} are rotated with respect to each other by comparatively large angles. The present work has shown that in all other cases considered there is little difficulty in distinguishing between distorted type 2 and type 3 images corresponding to $\underline{g} \cdot \underline{b} = 0$ and $|\underline{g} \cdot \underline{b}| = \frac{1}{2}$ or 1 for non-edge loops.

(b) No examples were found of images exhibiting type 4 contrast from loops within the layer structure being sufficiently modified so that they could be confused with images corresponding to $|\underline{g} \cdot \underline{b}| < 1$. In all cases the characteristic B-W interface structure is retained and, as will be shown in Part IV, this should always provide a firm basis for their positive identification.

(c) The results presented in this section together with comment (b) serve to emphasise the necessity of obtaining images in several reflections from a given loop to arrive at an unambiguous assignment of \underline{b} and \underline{n} .

3.4 Determination of loop Normal.

As well as determining \underline{b} it is clearly important to evaluate \underline{n} in order to define the geometry of non-edge loops. The images presented in figure 8 have already shown that the ℓ vector is not uniquely related to \underline{n} . In exploring alternative approaches to estimating \underline{n} we have examined two

features related to the change in image symmetry on going to non-edge loop geometries. First is the distortion of the type 2 "butterfly" images, giving them a strongly skewed appearance, when \underline{n} is rotated out of the \underline{b} - \underline{z} plane. This distortion occurs irrespective of whether or not \underline{n} lies in the image plane (figures 2(a) iii - vi, 4(b) iii - vi, 6(a) iv and vi). A striking feature of all these images is that the direction of skewing tends to lie along \underline{n} (or its projection in the image plane, \underline{n}_p). It is clear that on rotating \underline{n} from one side of \underline{b} to the other the strong black and white lobes switch sides with respect to the line of symmetry along \underline{g} e.g. see images iii and iv in figures 2(a) and 4(b). Thus, if sets of possible \underline{n} 's for non-edge loops are rotated out of the \underline{b} - \underline{z} plane and the \underline{n}_p 's are rotated with respect to each other they may be reliably distinguished from the direction of skewing of the distorted type 2 images. However, when \underline{n}_p is parallel to \underline{b} the type 2 image undergoes minimal change in symmetry making it virtually impossible to even distinguish between edge and non-edge loops (figures 6(a) iii, v, and vii).

The second feature we have investigated is the angular relationship between \underline{m} and \underline{n} (or \underline{n}_p), where \underline{m} defines the normal to the B-W interface in type 3 and type 4 images. In the case of type 4 images \underline{m} is drawn normal to the axis of the ellipse delineating the interface structure. The results for loops having $\underline{b} = \frac{a}{2} \langle 111 \rangle$ and $a \langle 100 \rangle$ at $\underline{z} = [\bar{0}11]$ and $\underline{b} = a \langle 100 \rangle$ at $\underline{z} = [\bar{0}01]$ are shown in figures 13, 14 and 15 respectively.

Considering first figure 13, the set of images included in (a) are for loops having $\underline{b} = \frac{a}{2} [\bar{1}1\bar{1}]$ normal to \underline{z} . The top row of images are for edge loops, the middle row for non-edge loops with \underline{n} remaining normal to \underline{z} , but rotated out of the \underline{b} - \underline{z} plane by $\sim 35^\circ$, i.e. $\underline{n} = [\bar{0}1\bar{1}]$ and the bottom row are for a second non-edge loop geometry with \underline{n} inclined to \underline{z} by 60° and rotated out of the \underline{b} - \underline{z} plane by $\sim 20^\circ$ i.e. $\underline{n} = [\bar{1}10]$. The striking feature

of these results is that \underline{m} is independent of \underline{g} and always coincides with \underline{n} . when both \underline{b} and \underline{n} lie in the image plane. Even when \underline{n} is inclined to the image plane \underline{m} is influenced slightly by \underline{g} but always lies close to \underline{n}_p . However, a rather different picture emerges from the set of images in figure 13(b) which are from loops having $\underline{b} = \frac{a}{2} [11\bar{1}]$ inclined by 35° to \underline{z} . Again, the top row of images correspond to the loop in its edge configuration and \underline{m} is only parallel to \underline{n}_p when \underline{g} , \underline{b}_p and \underline{n}_p are all coincident, but for the two $\langle 211 \rangle$ \underline{g} 's, rotated out of the \underline{b} - \underline{z} plane, \underline{m} is rotated towards \underline{g} . The second row of images correspond to non-edge loops with $\underline{n} = [01\bar{1}]$ parallel to \underline{z} and in this case \underline{m} is always parallel to \underline{g} . The third row of images correspond to the loop in a second non-edge configuration with $\underline{n} = [11\bar{0}]$ inclined to \underline{z} by 60° and rotated out of the \underline{b} - \underline{z} plane by $\sim 35^\circ$. Again \underline{m} is influenced by \underline{g} although for $\underline{g} = [200]$ and $[21\bar{1}]$ \underline{m} lies close to \underline{n}_p .

Going on to the second example illustrated in figure 14 the images are from both inclined and edge-on (with respect to the image plane) $a\langle 100 \rangle$ loops and a similar picture emerges as in the preceding example. The set of images included in figure 14(a) are for loops having $\underline{b} = a[01\bar{0}]$ inclined by 45° to \underline{z} in an edge configuration (first column) and lying on one of the possible $\{110\}$ nucleation planes (second, third and fourth columns). Considering first the images from the edge loops (first column), \underline{m} lies along \underline{n}_p for $\underline{g} = 01\bar{1}$ when \underline{g} , \underline{n}_p and \underline{b}_p are coincident and is rotated towards \underline{g} for the two $\langle 211 \rangle$ \underline{g} 's. The images from the loop in a non-edge configuration with $\underline{n} = [01\bar{1}]$ (second column in figure 14(a)) is an interesting case since \underline{n} is both normal to \underline{z} and lies in the \underline{b} - \underline{z} plane. In this case \underline{m} is virtually independent of \underline{g} and lies close to \underline{n} , although the black and white lobes are skewed markedly towards \underline{g} . When \underline{n} is parallel to \underline{z} i.e. $\underline{n} = [01\bar{1}]$ (third column of images in figure 14(a)) \underline{m} is again always close to \underline{g} . The fourth column of images in figure 14(a) is from a loop with $\underline{n} =$

$[110]$ inclined 60° to \underline{z} and rotated out of the \underline{b} - \underline{z} plane by $\sim 55^\circ$. For $\underline{g} = 01\bar{1}$, \underline{m} is rotated strongly towards \underline{n}_p , but for the other two \underline{g} 's the interface is zig-zag or wavy and it is not realistic to define an \underline{m} vector. With regard to the loops having $\underline{b} = a [100]$ normal to \underline{z} , figure 14(b) shows that type 4 images are obtained for the \underline{g} 's used ($\underline{g} \cdot \underline{b} = 0$ for $\underline{g} = 01\bar{1}$). For the edge loop configuration \underline{m} is always coincident with \underline{n} and independent of \underline{g} as expected. For the non-edge configuration with $\underline{n} = [110]$ inclined to \underline{z} by 60° and rotated out of the \underline{b} - \underline{z} plane by $\sim 35^\circ$ (second column of images) \underline{m} is rotated slightly towards \underline{g} but always lies close to \underline{n}_p .

The third example shown in figure 15 is for a loop having $\underline{b} = a [100]$ normal to $\underline{z} = [001]$ in the edge and two non-edge configurations. The top row of images correspond to the loop in its edge configuration and, as expected, \underline{m} is independent of \underline{g} and always coincides with \underline{n} . The middle row of images corresponds to the loop in a non-edge configuration with $\underline{n} = [110]$ both normal to \underline{z} and rotated out of the \underline{b} - \underline{z} plane by 45° and \underline{m} again always coincides with \underline{n} . The bottom row of images corresponds to the loop in a second non-edge configuration with $\underline{n} = [101]$ inclined 45° to \underline{z} but lying in the \underline{b} - \underline{z} plane and in this case \underline{m} is influenced slightly by \underline{g} but always lies close to \underline{n}_p .

The theoretical results predict therefore that the \underline{m} vector for $\underline{g} \cdot \underline{b} \neq 0$ images frequently gives a good estimate of \underline{n} or \underline{n}_p . More specifically, when \underline{b} and \underline{n} lie normal to \underline{z} , \underline{m} gives a precise determination of \underline{n} . Even for inclined loops when \underline{b} or \underline{n} are inclined by $> 45^\circ$ to \underline{z} , \underline{m} gives a reasonably close estimate of \underline{n}_p , so that it is often possible to clearly distinguish between perfect loops lying on different $\{110\}$ nucleation planes. Only when \underline{n} lies parallel or close to \underline{z} , is \underline{m} not related to \underline{n} , but even then the rotation of \underline{m} with \underline{g} gives a good indication that the \underline{n} is close to \underline{z} . We therefore conclude that \underline{m} vector analysis for B-W images

is a useful approach to determining \underline{n} for small dislocation loops and in Part IV we present some experimental examples illustrating its use for the analysis of loops in irradiated molybdenum.

4. General Discussion and Conclusions

The primary objective of carrying out the image calculations reported in this paper has been to provide a method for analysing experimental images from small dislocation loops in bcc metals. These are generally more complex than in fcc metals because of the early unfauling of $\frac{a}{2} \langle 110 \rangle$ faulted loops to one of two Burgers vectors resulting in many possible combinations of \underline{b} and \underline{n} . We present examples of how the present results can be applied to the analysis of small loops in irradiated bcc metals in Part IV. However, before doing this we point to some of the limitations of the present calculations and summarise the main conclusions on the approach to be adopted in matching theoretical and experimental images.

Considering first the limitations, the present calculations, like those in Part I, are restricted to dislocation loops in an elastically isotropic cubic metal. While this is a good approximation for metals such as W, Al, and Mo there are others such as α -Fe and Cu which exhibit comparatively high anisotropy, and so care must be taken when applying the results to these metals. Nevertheless, it was found in Part II that the theoretically simulated images closely match experimental images from loops in both Mo and Cu indicating that in the latter case, elastic anisotropy does not appear to have a significant effect on the image contrast.

The present work has also not considered how image contrast varies with loop position, particularly as the loop goes through a transition zone between layers. This was investigated in Part I and the important aspect exposed was that the simple B-W type 3 images corresponding to $0 < |\underline{g} \cdot \underline{b}| \leq 1$ can develop an interface structure if the loop is in a transition zone and

they could therefore be difficult to distinguish from type 4 ($|\underline{g}.\underline{b}| > 1$) layer images. However it was emphasised that the probability of loops being located in a transition zone is small. In Part II experimental evidence for such transition zone images was presented and it was also demonstrated that a simple test to establish whether or not a particular image arises from a loop located within a transition zone is to examine it with other diffraction vectors so that the dimensions of the layer structure are effectively changed. This test should be equally applicable to images from non-edge loops and thus the occurrence of transition zone images should not unduly complicate the use of simulated images for analysis of mixed populations of edge and non-edge loops.

The conclusions from the present work on the simulated images from non-edge loops are:-

(1) Modifications of the edge loop images are predicted on going to the non-edge configuration, but that in the majority of cases where $|\underline{g}.\underline{b}| = 1$ or $|\underline{g}.\underline{b}| > 1$ (types 3 and 4) the images retain their basic form with some skewing of the B-W lobes and rotation of the B-W interface. The degree of rotation of the interface can give an estimate of \underline{n} .

(2) It is emphasised that $|\underline{g}.\underline{b}| > 1$ images (type 4) always retain their characteristic interface structure between the black and white lobes.

(3) The $|\underline{g}.\underline{b}| = 0$ images from loops with \underline{b} normal to \underline{z} may be distorted significantly from the symmetrical 'butterfly' type 2 images for pure edge loops.

(4) For some specific combinations of \underline{g} , \underline{b} , \underline{n} and \underline{z} difficulty is encountered in distinguishing between modified type 1 and type 2 images ($|\underline{g}.\underline{b}| = 0$) and modified type 3 images corresponding to the conditions $0 < |\underline{g}.\underline{b}| < 1$.

(5) The direction of skewing of distorted type 2 images can often be used to distinguish between different families of \underline{n} 's rotated by different amounts out of the \underline{b} - \underline{z} plane.

(6) Provided \underline{n} and \underline{b} lie close to the image plane the vector \underline{m} provides a good estimate of \underline{n} . This estimate is very precise when both \underline{b} and \underline{n} lie in the image plane.

Turning to the application of the present results to the analysis of dislocation loop geometries, an essential requirement is that the image should be examined using a number of \underline{g} 's. Thus different values of $|\underline{g} \cdot \underline{b}|$ are obtained and this should enable an unambiguous determination of \underline{b} to be made for all non-edge as well as edge loops. This method is similar in principle to the so-called $|\underline{g} \cdot \underline{b}|$ analysis technique established for analysing dislocation line segments and resolvable loops. Loop normals are estimated from a combination of the direction of skewing of distorted type 2 images and noting the behaviour of \underline{m} with changing \underline{g} for types 3 and 4 images. If conditions can be achieved so that \underline{b} and \underline{n} lie in the image plane the \underline{m} vector provides a very precise estimate of \underline{n} . The application of these approaches to the analysis of mixed populations of loops in irradiated Mo is described in Part IV.

Acknowledgements

The authors wish to thank P.J. Fernbank and N.J. Beesley for considerable assistance in carrying out the computations and preparing the Figures. They are also particularly grateful to E. Jenkins for the photographic processing of the computed images.

References

- Bullough R, Maher D M, and Perrin R C., 1971. Phys. Stat. Solidi (b) 43, 689.
- Bullough R, and Newman R C., 1960. Phil. Mag. 5, 921.
- Eason G, Noble B, and Sneddon I N., 1955. Phil. Trans. Roy. Soc. A247, 259.
- English C A, Eyre B L, Bartlett A F, and Wadley H N G., 1977. Phil. Mag. 35, 533.
- English C A, Eyre B L, Holmes S M, and Perrin R C., 1978. Electron Diffraction 1927-1977. Proceedings of International Conference on Electron Diffraction, London. Sept. 1977. (Published Inst. of Phys. Conf. Ser., No. 41, p, 381).
- English C A, Eyre B L, and Holmes S M, 1979. AERE - R9308 (Part IV).
- Eyre B L., 1972. "Defects in Refractory Metals". (Mol: SCK/CEN), p. 311.
- Eyre B L, and Bullough R., 1965. Phil. Mag. 12, 31.
- Eyre B L, Maher D M, Perrin R C., 1974. Proc. 8th Int. Congress on Electron Microscopy Vol. 1 (Canberra: Australian Academy of Sciences), p. 436.
- Eyre B L, Maher D M and Perrin R C., 1977a. J. Physics. F. 7, 1359. (Part I), 1977b. J. Physics. F. 7, 1370, (Part II).
- Föll H, and Wilkens M., 1977. Phys. Stat. Solidi (a), 39, 561.
- Haussermann F, Wilkens M, and Rühle M., 1972. Phys. Stat. Solidi. 50, 445.
- Holmes S M, Eyre B L, English C A, and Perrin R C., 1978, Harwell Report AERE R9307.
- Holmes S M, Eyre B L, and Perrin R C., 1976. Proc. 6th Eur. Congress on Electron Microscopy, Vol. 1. (Jerusalem, Tal. International Publishing Company), p. 279.
- Howie A, and Whelan M J., 1961. Proc. R. Soc. A 263, 217.
- Howie A, and Basinski Z S., 1968. Phil. Mag. 17, 1039.
- Humphreys C J, and Hirsch P B., 1968., Phil. Mag. 18, 115.
- Jäger W, and Wilkens M., 1975., Phys. Stat. Solidi. 32, 89.
- Jenkins M L, English C A, and Eyre B L., 1978. Phil. Mag. 38, 97.
- Maher D M, Bullough R, and Perrin R C., 1971. Phys. Stat. Solidi. 43, 707.
- McIntyre K G., 1967. Phil. Mag. 15, 205.
- Ohr S M., 1972. Phil. Mag. 26, 1307.
- Ohr S M., 1976. Phys. Stat. Solidi. (a) 38, 553.
- Rühle M., 1967a. Phys. Stat. Solidi. 19, 263.
1967b. Phys. Stat. Solidi. 19, 279.
- Rühle M, Wilkens M, and Essmann U., 1965.. Phys. Stat. Solidi. 11, 819.
- Saldin D K, and Whelan M J., 1975. EMAG, (Inst. of Phys. Conf.), Bristol. p. 393.
- Wilkens M, and Rühle M., 1972. Phys. Stat. Solidi. 49, 749.

Appendix

Displacement field of a circular finite loop

A set of cartesian axes x_i is defined with its origin at the loop centre so that x_3 is along \underline{n} , and x_1 and x_2 define the loop plane such that x_1 is along the shear component of \underline{b} . If the sign convention given in Section 2.2 is employed and the components of \underline{b} are written in the x_i system, it can be seen that $b_1 \geq 0$, $b_2 = 0$ and b_3 is positive, negative or zero for the loop having vacancy, interstitial or pure shear nature respectively. Then the displacement field \underline{R} in the x_i system may be written (Bullough and Newman 1960, Ohr 1972)

$$r_1 = -x_1(f_1 + x_1 f_3) - f_4$$

$$r_2 = -x_2(f_1 + x_1 f_3)$$

$$r_3 = -f_2 - x_1 f_5$$

where

$$f_1 = \frac{b_3}{4(1-\nu)\rho a} \{ |\zeta| I_1^1 - (1-2\nu) I_1^0 \}$$

$$f_2 = \frac{b_3 |\zeta|}{4(1-\nu)\zeta} \{ |\zeta| I_0^1 + 2(1-\nu) I_0^0 \}$$

$$f_3 = \frac{b_1 \zeta}{4(1-\nu)\rho^3 a^2} \{ 2I_1^0 - \rho I_0^1 \}$$

$$f_4 = \frac{b_1 |\zeta|}{4(1-\nu)\zeta} \{ 2(1-\nu) I_0^0 - \frac{|\zeta|}{\rho} I_1^0 \}$$

$$f_5 = \frac{b_1}{4(1-\nu)\rho a} \{ |\zeta| I_1^1 + (1-2\nu) I_1^0 \}$$

a = loop radius

$$\rho = \frac{[x_1^2 + x_2^2]^{\frac{1}{2}}}{a}$$

$$\zeta = \frac{x_3}{a}$$

ν = Poisson's ratio

and
$$I_m^n = \int_0^\infty t^n J_1(t) J_m(\rho t) \exp(-|\zeta|t) dt$$

The integrals I_m^n may be expressed in terms of elliptic integrals as shown by Eason, Noble and Sneddon (1955).

The quantity required in the electron diffraction equations is $\underline{g} \cdot \underline{R} \frac{dr}{dz}$ or $-\underline{g} \cdot \frac{d\underline{R}}{dz}$ where \underline{z} is anti-parallel to the electron beam and \underline{g} lies in the plane normal to this. Another set of axes X_i is now defined such that the origin is at the loop centre and X_3 is in the \underline{z} direction. Then X_1 and X_2 define the co-ordinates of the columns and also the plane containing \underline{g} . Therefore, if \underline{R} has components R_i in the X_i system, the only terms required are R_1, R_2 , or $-\frac{dR_1}{dX_3}, -\frac{dR_2}{dX_3}$. A matrix \underline{U} is defined so that U_{ij} is the direction cosine between the axes X_i and x_j . Then the required components are

$$R_i = -(X_i - U_{i3}x_3)(f_1 + x_1f_3) - U_{i3}(f_2 + x_1f_5) - U_{i1}f_4$$

and
$$\frac{dR_i}{dX_3} = -(X_i - U_{i3}x_3)\left(\frac{df_1}{dX_3} + U_{31}f_3 + x_1\frac{df_3}{dX_3}\right) - U_{i3}\left(\frac{df_2}{dX_3} + U_{31}f_5 + x_1\frac{df_5}{dX_3} - U_{33}(f_1 + x_1f_3)\right) - U_{i1}\frac{df_4}{dX_3} \quad (i = 1, 2)$$

where
$$\frac{df_1}{dX_3} = \frac{b_3(X_3 - U_{33}x_3)}{4(1-\nu)a^3\rho^3} \{2(1-2\nu)I_1^0 - 2|\zeta|I_1^1 - \rho[(1-2\nu)I_0^1 - |\zeta|I_0^2]\} + \frac{b_3U_{33}|\zeta|}{4(1-\nu)a^2\rho\zeta} \{2(1-\nu)I_1^1 - |\zeta|I_1^2\}$$

$$\frac{df_2}{dX_3} = \frac{-b_3(X_3 - U_{33}x_3)}{4(1-\nu)a^2\rho} \frac{|\zeta|}{\zeta} \{2(1-\nu)I_1^1 + |\zeta|I_1^2\} - \frac{b_3U_{33}}{4(1-\nu)a} \{(1-2\nu)I_0^1 + |\zeta|I_0^2\}$$

$$\frac{df_3}{dX_3} = \frac{b_1(X_3 - U_{33}x_3)}{4(1-\nu)a^4\rho^5} \zeta \{4\rho I_0^1 - 8I_1^0 + \rho^2 I_1^2\} + \frac{b_1U_{33}}{4(1-\nu)a^3\rho^3} \{2I_1^0 - \rho I_0^1 - 2|\zeta|I_1^1 + \rho|\zeta|I_0^2\}$$

$$\frac{df_4}{dX_3} = \frac{b_1(X_3 - U_{33}X_3)}{4(1-\nu)a^2\rho^3} \{ 2I_1^0 - \rho I_0^1 - \frac{2(1-\nu)}{|\zeta|} \rho^2 I_1^1 \} + \frac{b_1 U_{33}}{4(1-\nu)a\rho} \{ |\zeta| I_1^1 - I_1^0 - 2\rho(1-\nu)I_0^1 \}$$

$$\frac{df_5}{dX_3} = \frac{b_1(3 - U_{33}X_3)}{4(1-\nu)a^3\rho^3} \{ \rho(1-2\nu)I_0^1 + \rho|\zeta|I_0^2 - 2(1-2\nu)I_1^0 - 2|\zeta|I_1^1 \} + \frac{b_1 U_{33}}{4(1-\nu)a^2\rho} \frac{|\zeta|}{\zeta} \{ 2\nu I_1^1 - |\zeta|I_1^2 \}$$

All the I_m^n required for $\frac{dR_i}{dX_3}$ may be written in terms of complete elliptic integrals of the first and second kind; however, to calculate I_0^0 in R_i incomplete elliptic integrals are also required, and the extra time used for this makes $\frac{dR_i}{dX_3}$ quicker to compute despite the greater complexity of the expressions, as mentioned in section 2.1.

In the program for pure edge loops described by Bullough, Maher and Perrin (1971) two simplifications were made in computing $\frac{dR_i}{dX_3}$: firstly, at large distances from the loop the displacement field of an infinitesimal loop was used, and secondly, the I_m^n were tabulated for various ρ and $|\zeta|$, and the nearest result to the required point used. Because of the time saved in the Bloch-wave program, neither of these approximations is used; the finite loop displacement field is calculated afresh at each point in the integration using supplied computer library subroutines for the elliptic integrals. The above expressions may be reduced to those for an infinitesimal loop if required by making the approximation

$$\frac{r^2}{a^2} = \rho^2 + |\zeta|^2 \sim (1+\rho)^2 + |\zeta|^2$$

and using well-known expansions for the elliptic integrals. Then, for example,

$$I_0^1 \sim \frac{a^3}{r^3} \left(1 - \frac{3\rho^2 a^2}{2r^2} \right)$$

One final point which requires some care in programming is the behaviour of the displacement field as $\rho \rightarrow 0$, which apparently diverges from the above expressions for f and $\frac{df}{dx_3}$. It can be shown that this is not the case by again expanding the elliptic integrals, this time in the limit of small ρ for various combinations of the I_m^n . For example,

$$\left[\frac{I_1^0}{\rho} \right]_{\rho=0} = \frac{1}{2(1+|\zeta|^2)^{3/2}} \quad \text{and} \quad [I_0^1]_{\rho=0} = \frac{1}{(1+|\zeta|^2)^{3/2}}$$

but

$$\left[\frac{2I_1^0}{\rho^3} - \frac{I_0^1}{\rho^2} \right]_{\rho=0} = \frac{3(4|\zeta|^2-1)}{8(1+|\zeta|^2)^{7/2}}$$

Rather than separately compute such expressions as $\rho \rightarrow 0$, it is easier in practice to avoid such problems by moving the grid of columns slightly to minimise the number that intersect the loop normal, and to set ρ equal to some small value ϵ for all $\rho < \epsilon$.

TABLE 1

Contrast parameters (100 kV electrons)

$\epsilon_0(\text{\AA})^+$	$\epsilon'_g(\text{\AA})^\ddagger$
$\epsilon_{110} = 232$	$\epsilon'_{110} = \epsilon_{110}/0.06$
$\epsilon_{200} = 329$	$\epsilon'_{200} = \epsilon_{200}/0.08$
$\epsilon_{211} = 411$	$\epsilon'_{211} = \epsilon_{211}/0.1$

⁺Howie & Bansinski (1968).

[‡]Humphreys & Hirsch (1968).

TABLE 2

Values of moduli of $g \cdot b$ for perfect and faulted loops at $z = [011]$ and $z = [001]$ in BCC Crystals

(a) $z = [011]$

$g \rightarrow$	$[01\bar{1}]$	$[21\bar{1}]$	$[200]$	$[2\bar{1}1]$
$b \uparrow$	$ g \cdot b $			
$\frac{a}{2} [01\bar{1}]$	1	1	0	1
$\frac{a}{2} [011]$	0	0	0	0
$\frac{a}{2} [\bar{1}10]$	$\frac{1}{2}$	$\frac{1}{2}$	1	$1\frac{1}{2}$
$\frac{a}{2} [110]$	$\frac{1}{2}$	$1\frac{1}{2}$	1	$\frac{1}{2}$
$\frac{a}{2} [101]$	$\frac{1}{2}$	$\frac{1}{2}$	1	$1\frac{1}{2}$
$\frac{a}{2} [\bar{1}\bar{1}1]$	1	0	1	2
$\frac{a}{2} [\bar{1}11]$	0	1	1	1
$a [100]$	0	2	2	2
$a [010]$	1	1	0	1

(b) $z = [001]$

$g \rightarrow$	$[\bar{1}10]$	$[020]$	$[\bar{1}10]$	$[200]$
$b \uparrow$	$ g \cdot b $			
$\frac{a}{2} [101]$	$\frac{1}{2}$	0	$\frac{1}{2}$	1
$\frac{a}{2} [110]$	0	1	1	1
$\frac{a}{2} [011]$	$\frac{1}{2}$	1	$\frac{1}{2}$	0
$a [010]$	1	2	1	0
$a [001]$	0	0	0	0

TABLE 3

Image Classification for Edge Loops within the Layer Structure ($W_g \sim 0$)

Image Type	Diffracting Conditions	Predicted Image
1	$\underline{g} \cdot \underline{b} = 0$ and $\angle (\underline{z}, \underline{n}) \leq 45^\circ$	Invisible or weak black/white lobes
2	$\underline{g} \cdot \underline{b} = 0$ and $\angle (\underline{z}, \underline{n}) \sim 90^\circ$	'Butterfly' contrast
3	$0 < \underline{g} \cdot \underline{b} \leq 1$	Simple black/white lobes
4	$ \underline{g} \cdot \underline{b} > 1$	Black/white lobes with interfaced structure

TABLE 4a
Figures showing Case (I) Images from Edge Loops

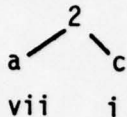
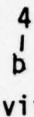
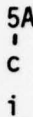
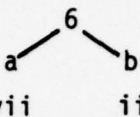

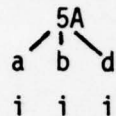
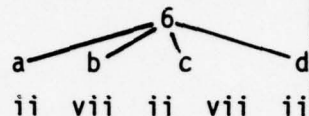
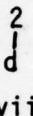
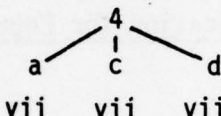
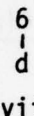
$ \underline{g.b} $		Figures			
0	Figure No. Column Image				
$0 < \underline{g.b} \leq 1$	Figure No. Column Image				
$ \underline{g.b} > 1$	Figure No. Column Image				

TABLE 4b
Figures showing Case (I) Images from Non-Edge Loops

$ \underline{g.b} $		Figures			
0	Figure No. Column Image	<div><div>2</div><div> </div><div>a</div></div> <div>iii v</div>		<div><div>6</div><div> </div><div>a</div></div> <div>iv vi</div>	
$0 < \underline{g.b} \leq 1$	Figure No. Column Image	<div><div>2</div><div>↙ ↘</div><div>b c</div></div> <div>iii v iii v</div>		<div><div>6</div><div>↙ ↘</div><div>b c</div></div> <div>iv vi iv vi</div>	
$ \underline{g.b} > 1$	Figure No. Column Image	<div><div>2</div><div> </div><div>d</div></div> <div>iii v</div>		<div><div>6</div><div> </div><div>d</div></div> <div>iv vi</div>	

TABLE 5
Figures showing Case (II) Images from Non-Edge Loops

$ \underline{g.b} $		Figures
0	Figure No. Column Image	<div style="display: flex; justify-content: space-around; align-items: flex-start;"> <div style="text-align: center;"> <p>2</p> <p> </p> <p>a</p> <p>iv vi iii v iv vi iii v</p> </div> <div style="text-align: center;"> <p>4</p> <p> </p> <p>b</p> </div> <div style="text-align: center;"> <p>5A</p> <p> </p> <p>c</p> </div> <div style="text-align: center;"> <p>6</p> <p> </p> <p>a</p> <p>iii v</p> </div> </div>
$0 < \underline{g.b} \leq 1$	Figure No. Column Image	<div style="display: flex; justify-content: space-around; align-items: flex-start;"> <div style="text-align: center;"> <p>2</p> <p> / </p> <p>b c</p> <p>iv vi iv vi iii iii iii iii iii v</p> </div> <div style="text-align: center;"> <p>5A</p> <p> / </p> <p>a b d</p> </div> <div style="text-align: center;"> <p>6</p> <p> / </p> <p>b c</p> <p>iii v iii v</p> </div> </div>
$ \underline{g.b} > 1$	Figure No. Column Image	<div style="display: flex; justify-content: space-around; align-items: flex-start;"> <div style="text-align: center;"> <p>2</p> <p> </p> <p>d</p> <p>iv vi iii v iv vi iii v iv vi iii v</p> </div> <div style="text-align: center;"> <p>4</p> <p> / </p> <p>a c d</p> </div> <div style="text-align: center;"> <p>6</p> <p> </p> <p>d</p> <p>iii v</p> </div> </div>

TABLE 6b
Figures showing Case (III) Images from Non-Edge Loops

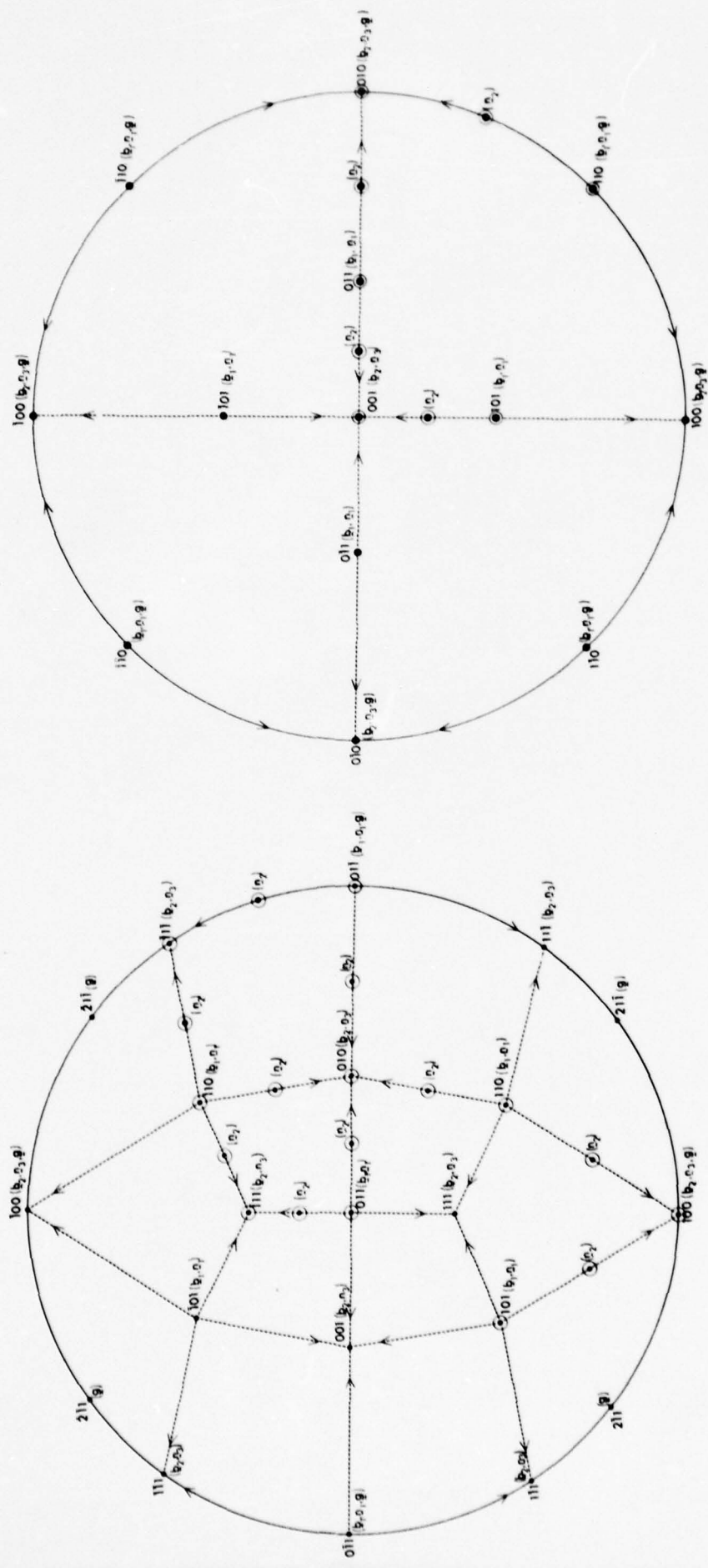
$ \underline{g.b} $	Figures	
0	Figure No. Column Image	<div style="display: flex; justify-content: space-around; align-items: center;"> <div style="text-align: center;"> $\begin{matrix} 3 \\ \\ a \end{matrix}$ v iv vi </div> <div style="text-align: center;"> $\begin{matrix} 5A \\ \\ c \end{matrix}$ v vi </div> <div style="text-align: center;"> $\begin{matrix} 5B \\ \\ c \end{matrix}$ v iv vi </div> </div>
$0 < \underline{g.b} \leq 1$	Figure No. Column Image	<div style="display: flex; justify-content: space-around; align-items: center;"> <div style="text-align: center;"> $\begin{matrix} b & & 3 \\ & \diagup & \\ & c & d \end{matrix}$ v iv vi </div> <div style="text-align: center;"> $\begin{matrix} & & 5A \\ & \diagdown & \\ a & b & d \end{matrix}$ v vi </div> </div>
$0 < \underline{g.b} \leq 1$	Figure No. Column Image	<div style="display: flex; justify-content: space-around; align-items: center;"> <div style="text-align: center;"> $\begin{matrix} a \\ \\ b \end{matrix}$ iii v iv vi </div> <div style="text-align: center;"> $\begin{matrix} 5B \\ \\ b \end{matrix}$ iii v iv vi </div> <div style="text-align: center;"> $\begin{matrix} d \\ \\ b \end{matrix}$ iii v iv vi </div> </div>

TABLE 7
Figures showing Case (IV) Images from Non Edge Loops

$ g.b $	Figures	
0	Figure No. Column Image	<div> <div>3 i a iii</div> <div>5A c iv</div> </div>
$0 < g.b \leq 1$	Figure No. Column Image	<div> <div>3 b iii</div> <div>5A a iv</div> </div>

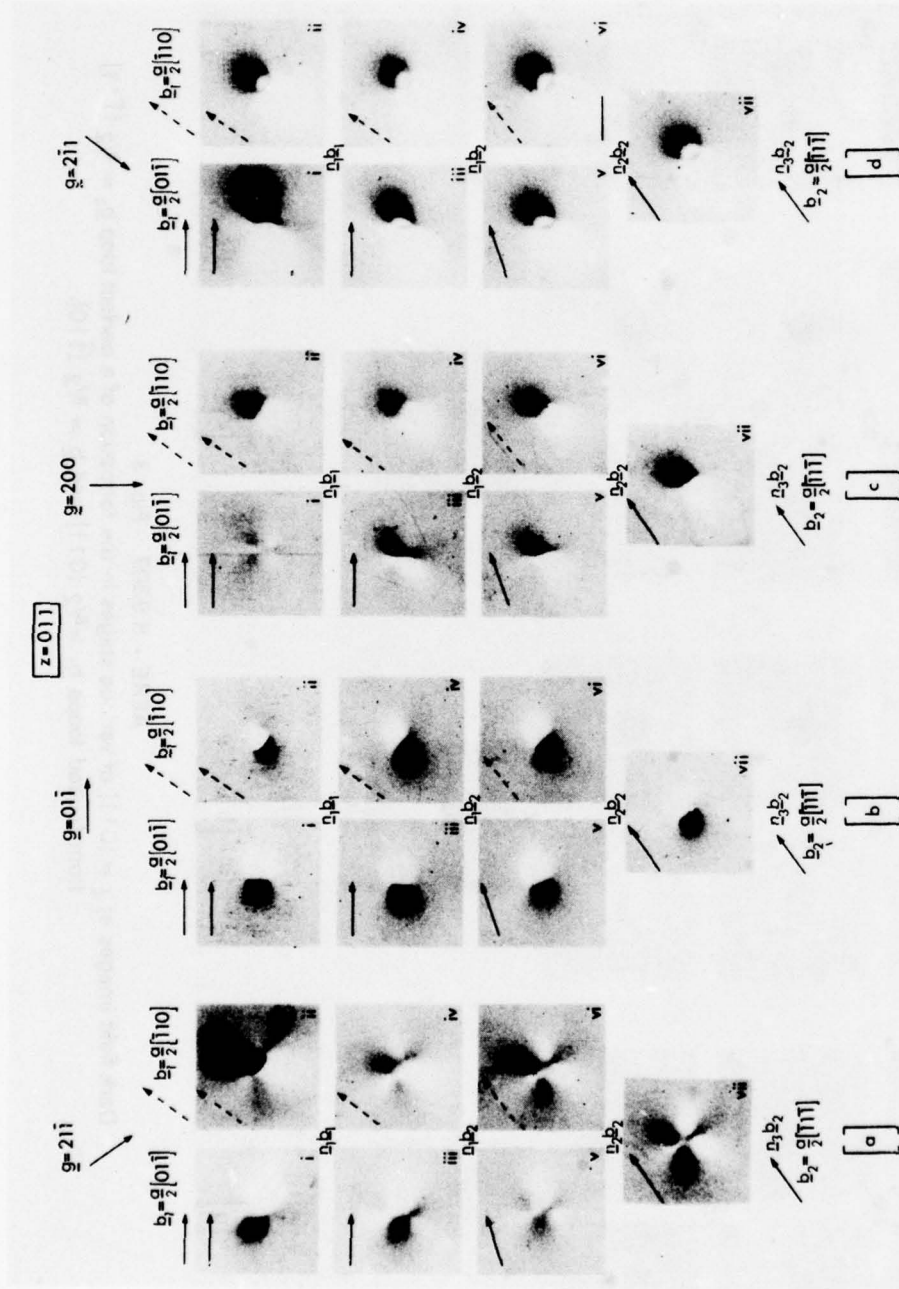
TABLE 8
Figures showing Case (V) Images from Edge Loops

$ g.b $	Figures	
0	Figure No. Column Image	<div> <div>3 a i</div> <div>5A b ii</div> </div>



AERE - R.9307 Fig. 1

(a) Stereographic projections illustrating the crystallographic relationships between the possible Burgers vectors (b_i), loop normal (n_i), and the diffracting vectors (g) under consideration in a B.C.C. crystal with (a) $z = [011]$ and (b) $z = [001]$. The symbol \odot specifies dislocation loops whose images are shown in figures 2-7.

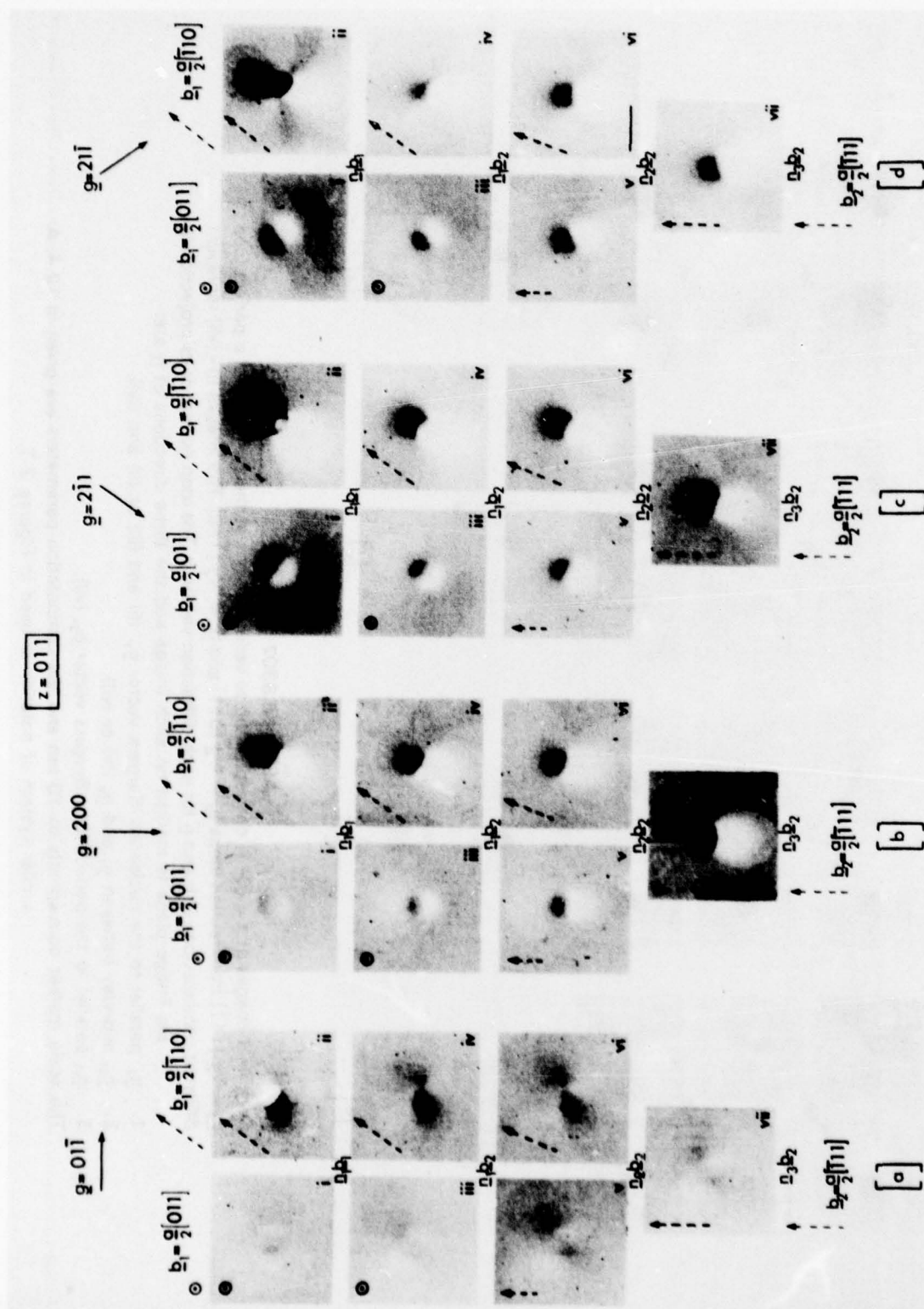


AERE - R.9307 Fig. 2

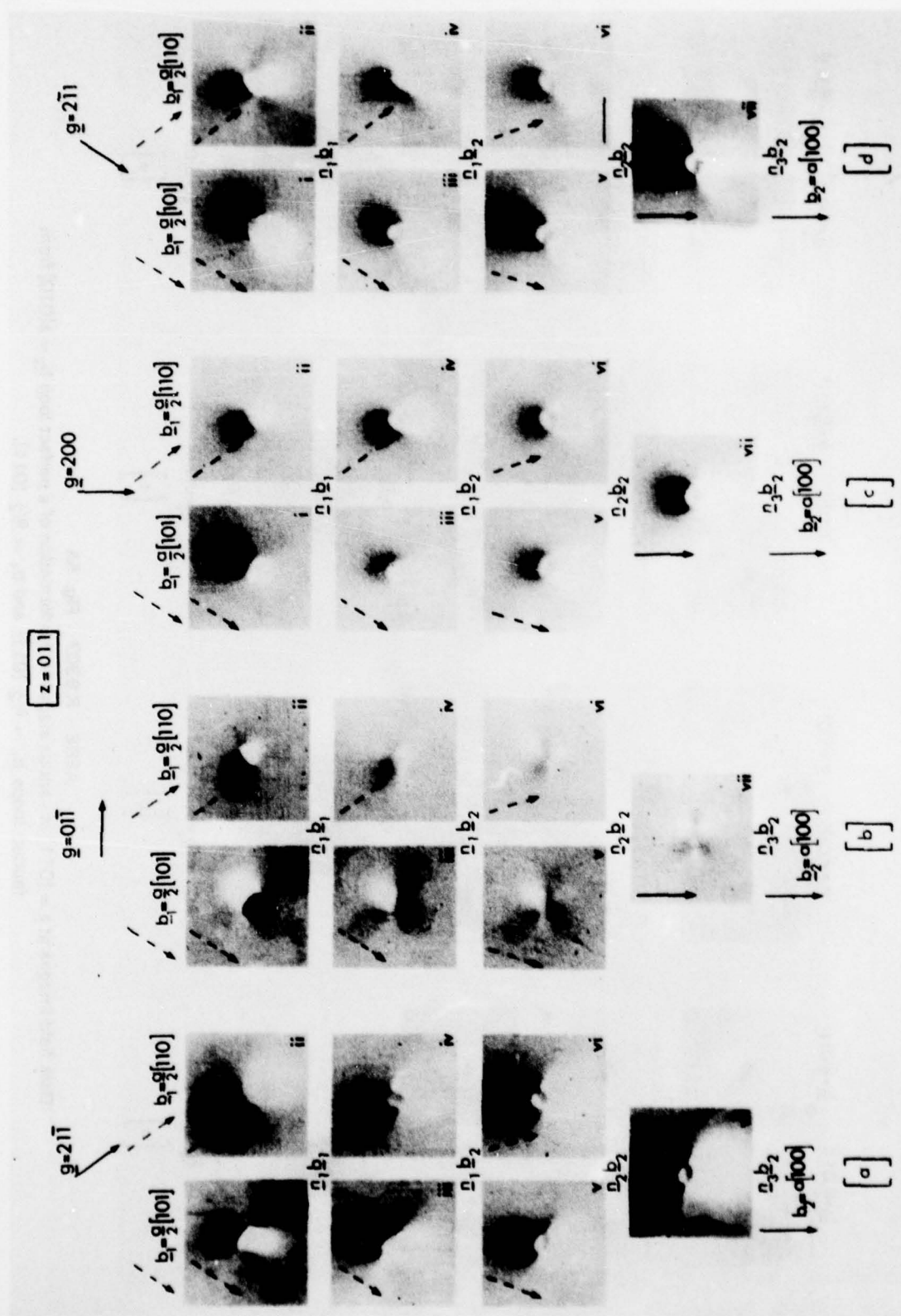
Dark field images at $z = [011]$ corresponding to various stages in the formation of a perfect loop $\underline{b}_2 = a/2 [111]$ from faulted loops $\underline{b}_1 = a/2 [011]$ and $\underline{b}_1 = a/2 [110]$. The images (i) - (vii) represent different combinations of \underline{b} and \underline{n} for each diffraction vector, g . The loop normal or its projection in the image plane is marked on each image \underline{b}_1 , (ii) and (iii) or (iv).

1. \underline{n}_1 , parallel to the nucleation Burgers vector \underline{b}_1 , (ii) and (iii) or (iv).
2. \underline{n}_2 , mid-way between \underline{n}_1 and \underline{n}_3 (v) or (vi).
3. \underline{n}_3 , parallel to the perfect loop Burgers vector \underline{b}_2 , (vii).

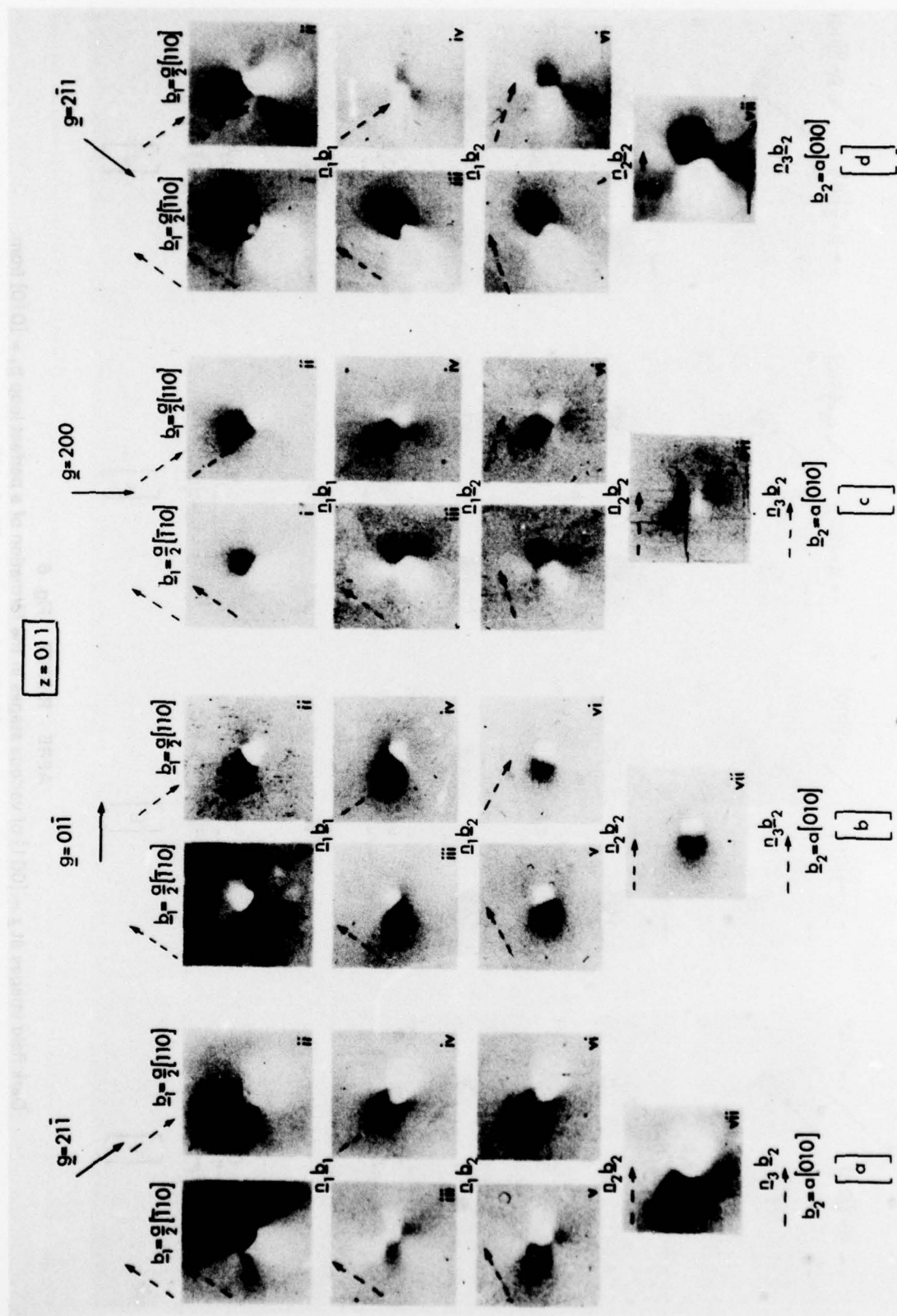
The scale marker corresponds to 10 nm and the computation parameters are given in §2.4. A similar system of notation is used in Figures 3-7.



AERE - R.9307 Fig. 3
Dark field images at $z = [011]$ of various stages in the formation of a perfect loop $b_2 = a/2 [111]$ from faulted loops $b_1 = a/2 [011]$ and $b_2 = a/2 [110]$.

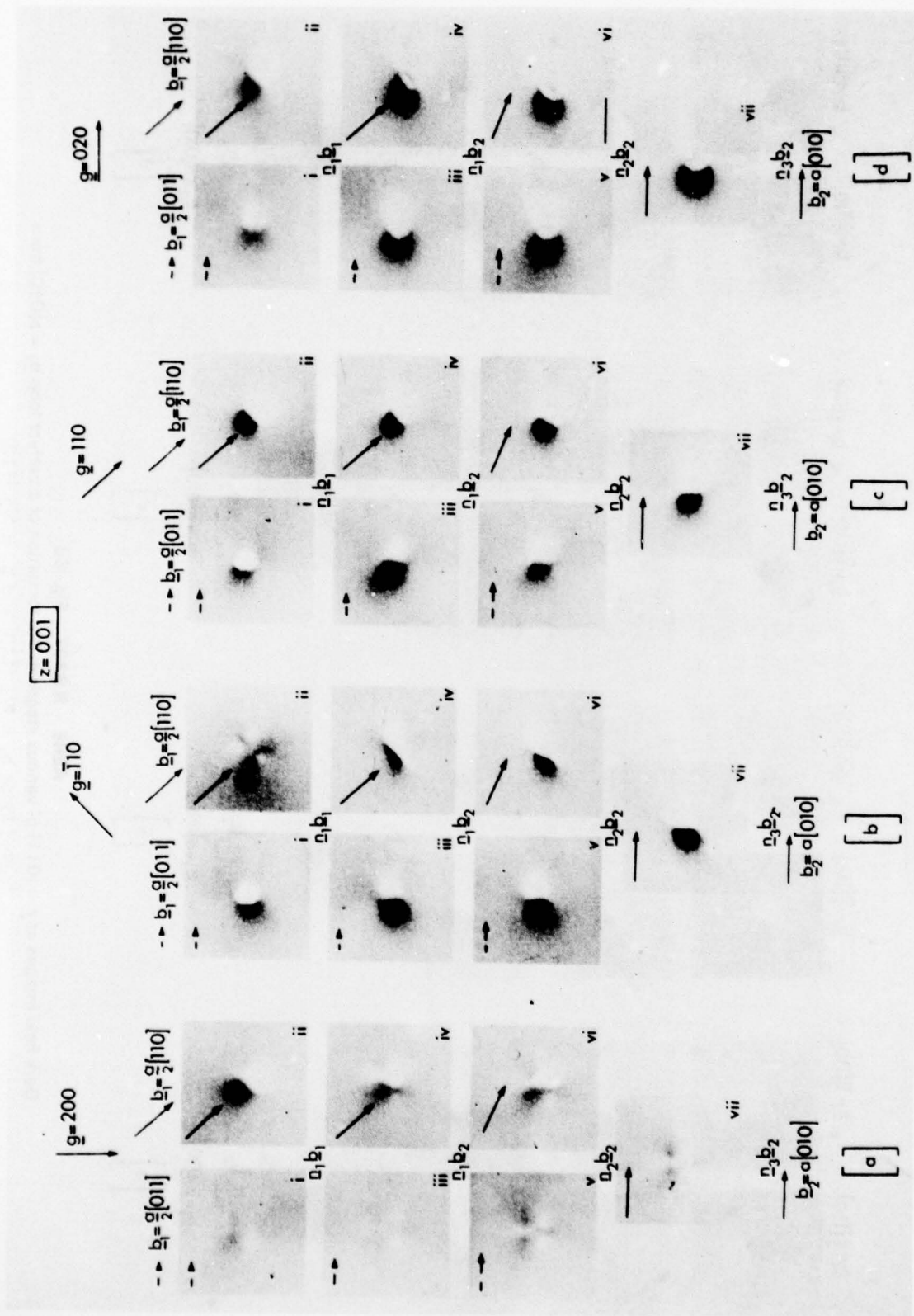


AERE - R.9307 Fig. 4
Dark field images at $z = [011]$ of various stages in the formation of a perfect loop $b_2 = a[100]$ from faulted loops $b_1 = a/2[101]$ and $b_1 = a/2[110]$.

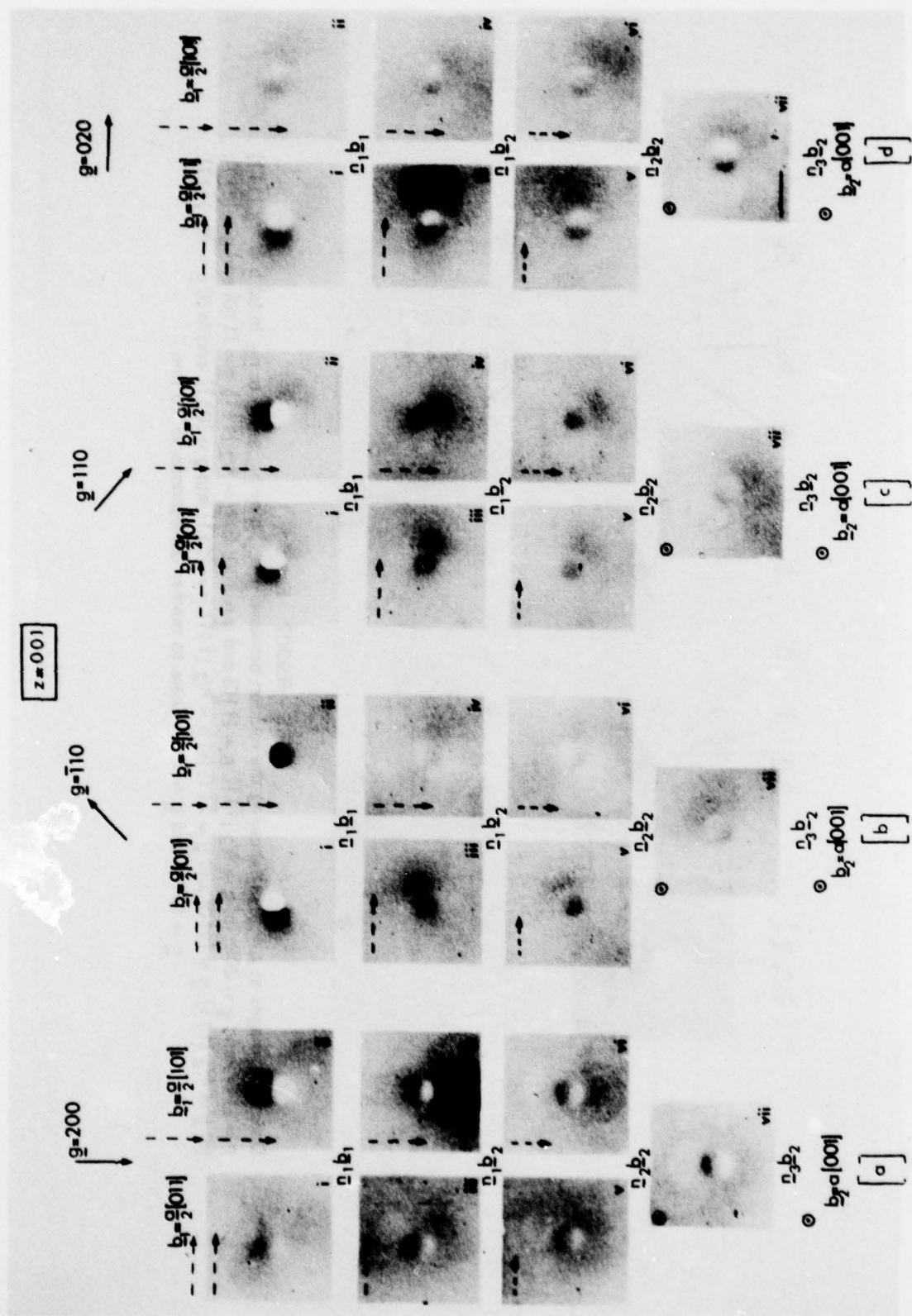


AERE - R.9307 Fig. 5B

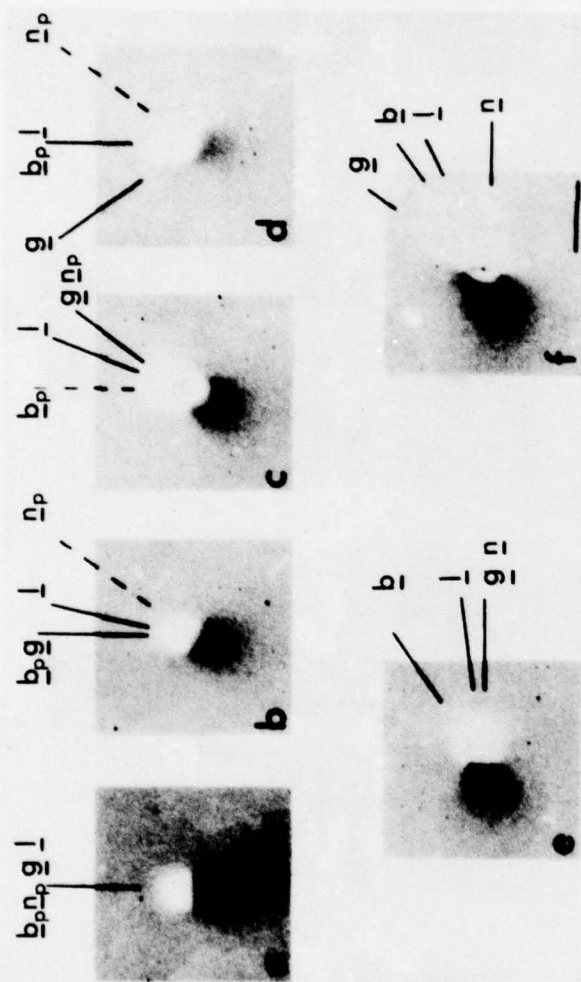
Dark field images at $z = [011]$ of various stages in the formation of a perfect loop $b_2 = a[010]$ from faulted loops $b_1 = a/2 [110]$ and $b_1 = a/2 [110]$.



AERE - R.9307 Fig. 6
Dark field images at $z = [001]$ of various stages in the formation of a perfect loop $b_2 = [010]$ from faulted loops $b_1 = a/2 [011]$ and $b_1 = a/2 [110]$.

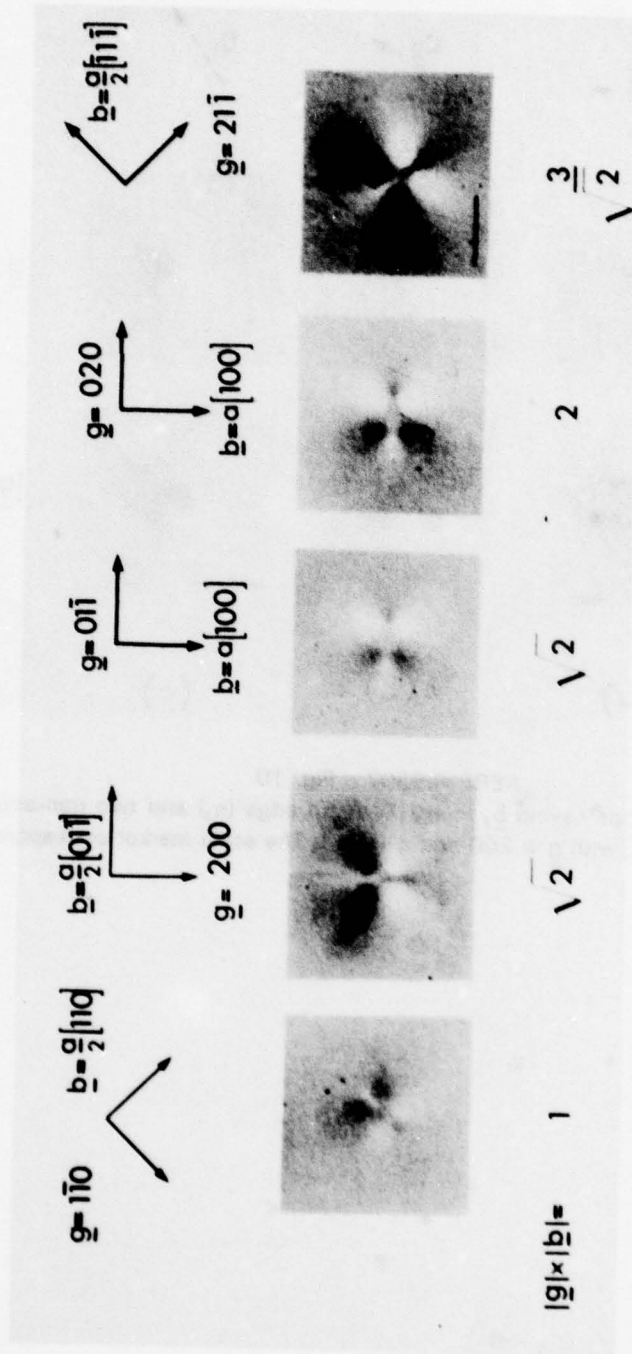


AERE - R.9307 Fig. 7
Dark field images at $z = [001]$ of various stages in the formation of a perfect loop $b_2 = [001]$ from faulted loops $b_1 = \frac{a}{2} [011]$ and $b_2 = [101]$.

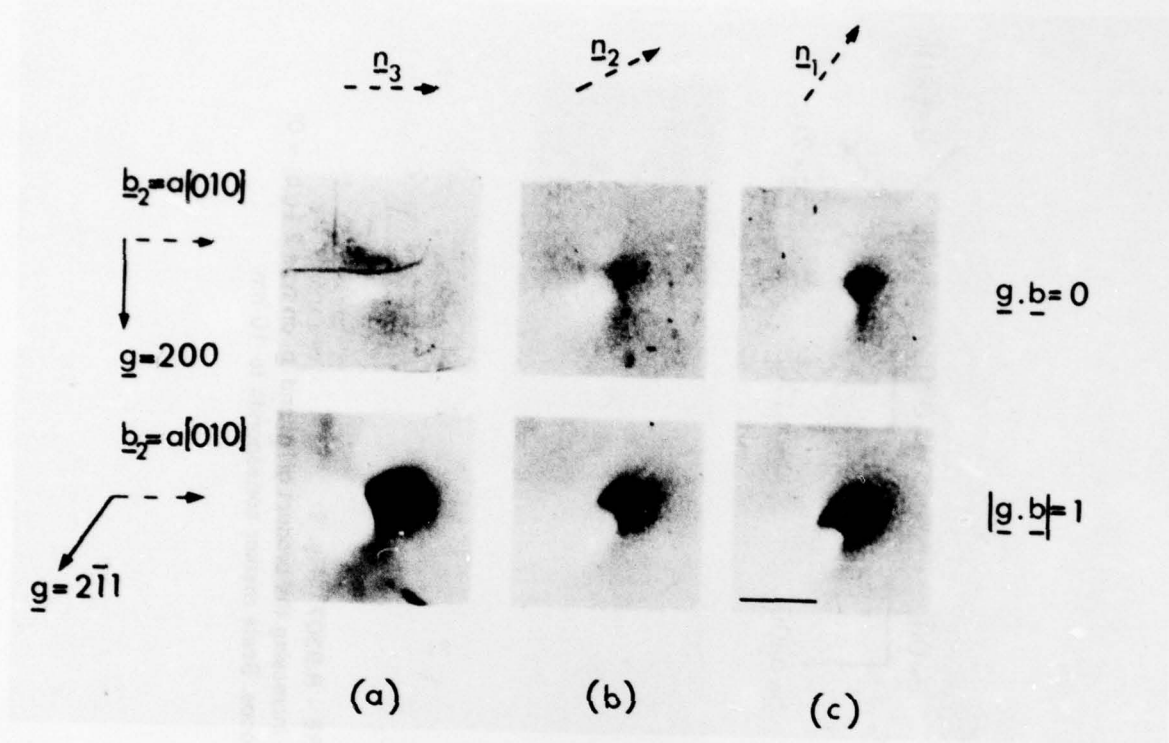


AERE - R.9307 Fig. 8

Dark field images at $z = [011]$ showing the relation between \underline{g} , \underline{g} , \underline{b} or \underline{b} , and \underline{n} or \underline{n} . In (a) $\underline{b} = \frac{a}{2} [\bar{1}11]$, $\underline{n} = [\bar{1}11]$ and $\underline{g} = 200$; (b) $\underline{b} = \frac{a}{2} [\bar{1}11]$, $\underline{n} = [110]$ and $\underline{g} = 200$; (c) $\underline{b} = \frac{a}{2} [\bar{1}11]$, $\underline{n} = [\bar{1}10]$ and $\underline{g} = [211]$; (d) $\underline{b} = \frac{a}{2} [\bar{1}11]$, $\underline{n} = [\bar{1}10]$ and $\underline{g} = 211$; (e) $\underline{b} = \frac{a}{2} [\bar{1}11]$, $\underline{n} = [011]$ and $\underline{g} = [011]$, and in (f) $\underline{b} = \frac{a}{2} [\bar{1}11]$, $\underline{n} = [011]$ and $\underline{g} = 211$. Scale to marker corresponds to 10 nm.

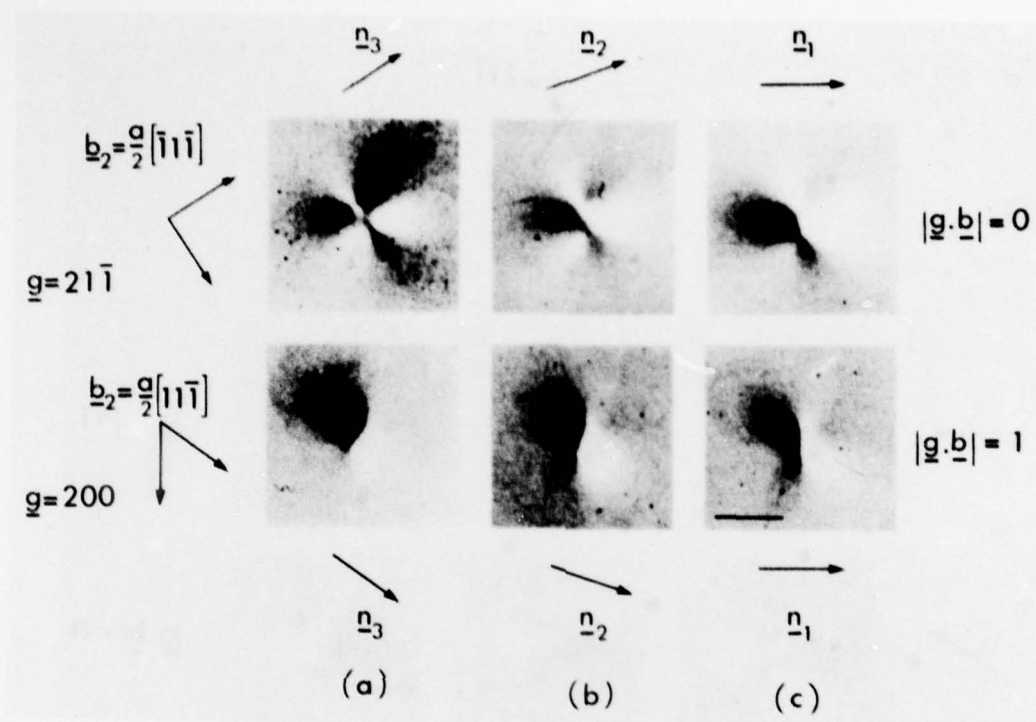


AERE - R.9307 Fig. 9
Dark field images showing the effect of increasing the product of $|\mathbf{g}|$ and $|\mathbf{b}|$ on type 2 ($\mathbf{g} \cdot \mathbf{b} = 0$) images from pure edge loops. Scale marker corresponds to 10 nm.



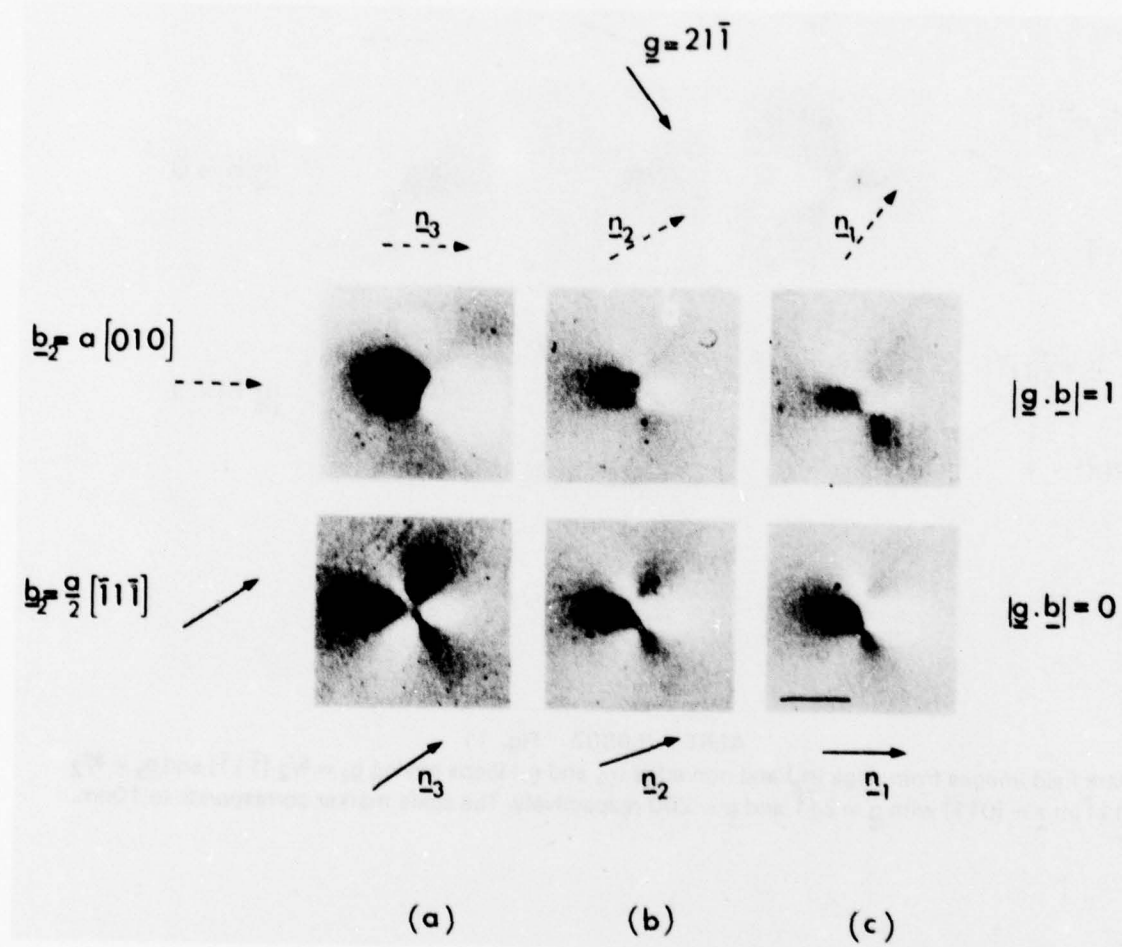
AERE R.9307 Fig. 10

Dark field images from loops having $\underline{b}_2 = a[010]$ in an edge (\underline{n}_3) and two non-edge (\underline{n}_2 and \underline{n}_1) configurations at $\underline{z} = [011]$ with $\underline{g} = 200$ and $\underline{g} = 2\bar{1}1$. The scale marker corresponds to 10 nm.



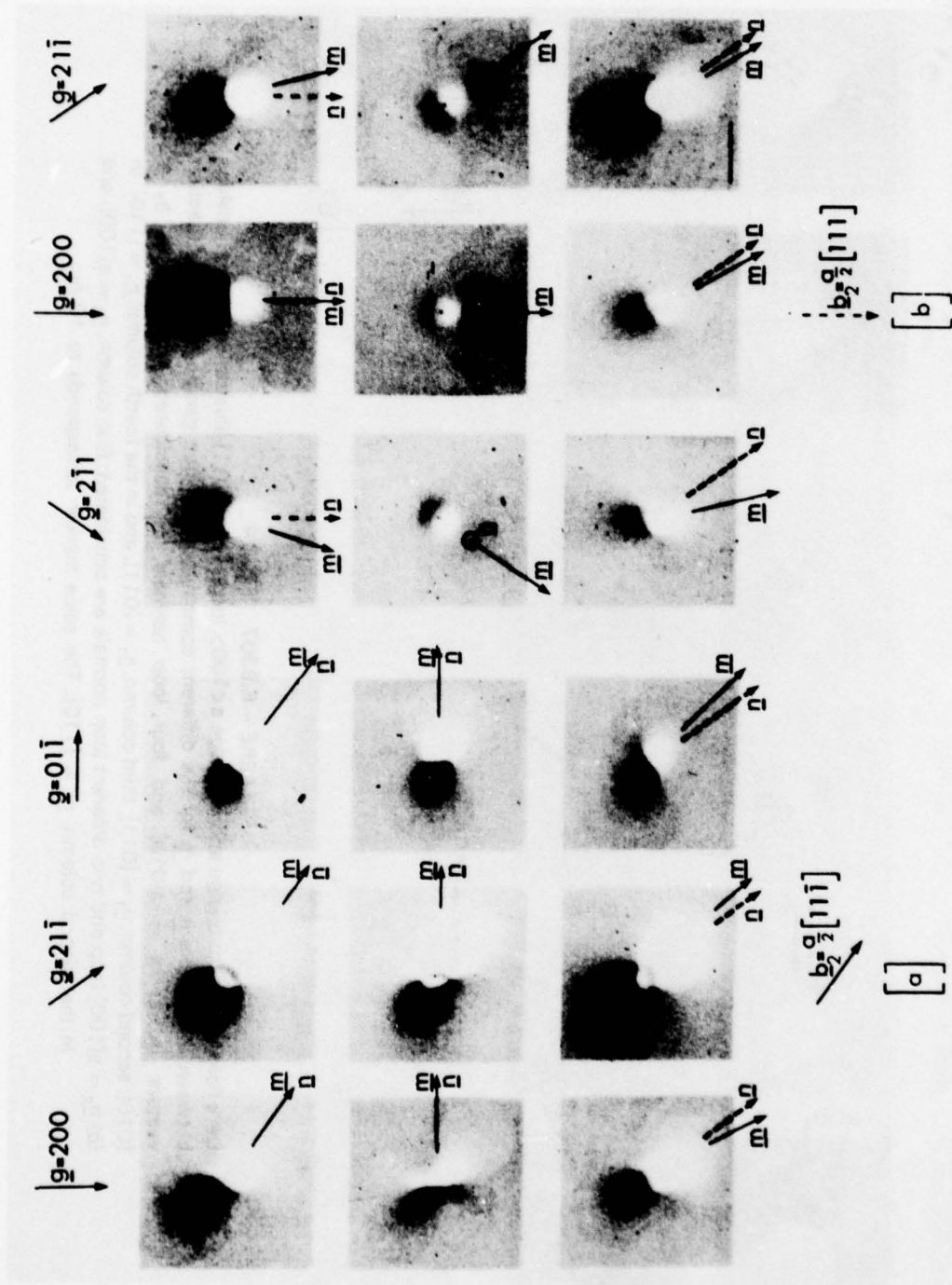
AERE - R.9307 Fig. 11

Dark field images from edge (n_3) and non edge (n_2 and n_1) loops having $b_2 = \frac{a}{2} [\bar{1}1\bar{1}]$ and $b_2 = \frac{a}{2} [11\bar{1}]$ at $z = [011]$ with $g = 21\bar{1}$ and $g = 200$ respectively. The scale marker corresponds to 10nm.



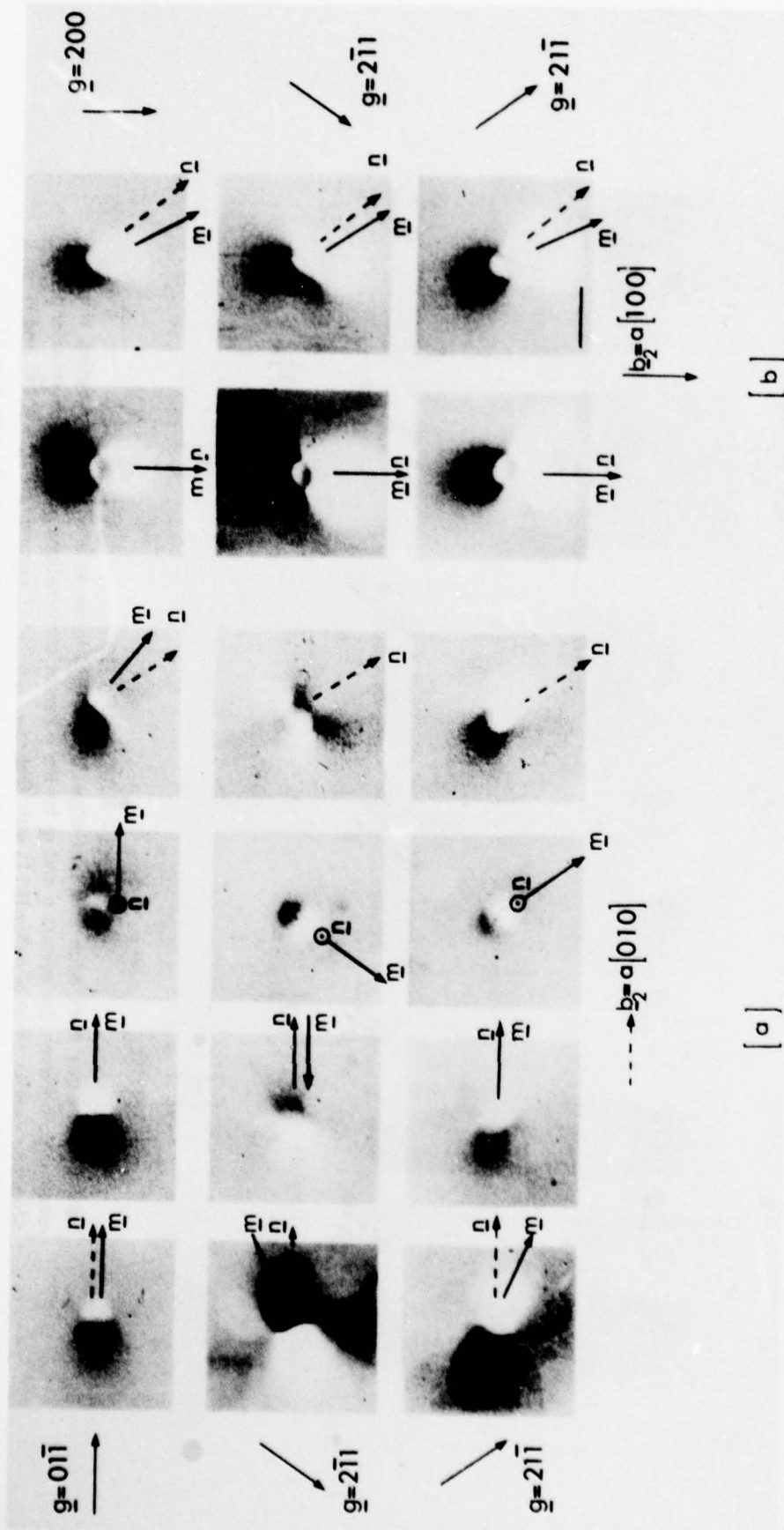
AERE - R.9307 Fig. 12

Dark field images from edge (\underline{n}_3) and non-edge (\underline{n}_1 and \underline{n}_2) loops having $\underline{b}_2 = a[010]$ and $\underline{b}_2 = \frac{a}{2}[\bar{1}1\bar{1}]$ at $z = [011]$ with $\underline{g} = 21\bar{1}$. The scale marker corresponds to 10 nm.



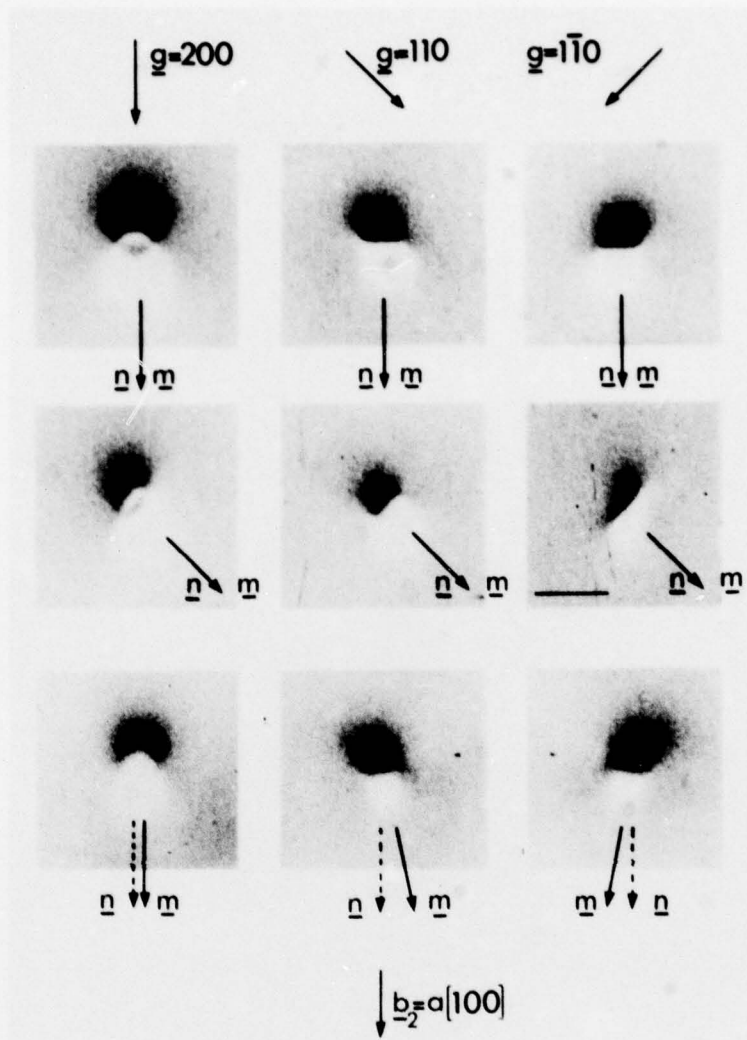
AERE - R.9307 Fig. 13

Dark field images from edge and non edge $a/2 < 111 >$ loops at $z = [011]$ illustrating the relationship between the vectors \underline{n} and \underline{m} for the different combinations of loop geometries and diffraction vectors. In (a) $\underline{b}_2 = a/2 [111]$ with: first row, $\underline{n}_3 = [111]$, second row, $\underline{n}_1 = [011]$, and in the third row, $\underline{n}_1 = [110]$. In (b) $\underline{b}_2 = a/2 [111]$ with: first row, $\underline{n}_3 = [111]$, second row, $\underline{n}_1 = [011]$ and in the third row, $\underline{n}_1 = [110]$. The scale marker corresponds to 10 nm.



AERE - R.9307 Fig. 14

Dark field images from edge and non edge $a\langle 100 \rangle$ loops at $z = [011]$ illustrating the relationships between the vectors \underline{n} and \underline{m} for the different combinations of loop geometries and diffraction vectors. In (a) $\underline{b}_2 = a[010]$ and four loop normals are considered: first column, $\underline{n}_1 = [010]$, second column, $\underline{n}_2 = [011]$, third column, $\underline{n}_3 = [110]$, and in the fourth column, $\underline{n}_4 = [110]$. In (b) $\underline{b}_2 = a[100]$ loop and two different loop normals are considered: first column, $\underline{n}_1 = a[100]$, and in the second column, $\underline{n}_2 = [110]$. The scale marker corresponds to 10 nm.



AERE - R.9307 Fig. 15

Dark field images from edge and non edge loops with $\underline{b}_2 = a[100]$ at $\underline{z} = [001]$ illustrating the relationships between the vectors \underline{n} and \underline{m} for the different combinations of loop geometries and diffraction vectors. Three loop normals are considered: top row, $\underline{n}_3 = [100]$, middle row, $\underline{n}_1 = [100]$, and in the bottom row $\underline{n}_1 = [101]$. The scale marker corresponds to 10 nm.